Boundary-Value PDEs Meet Higher-Order Differential Topology-aware GNNs

Yunfeng Liao **Yangxin Wu** **Xiucheng Li***
School of Computer Science and Technology, Harbin Institute of Technology (Shenzhen)
lixiucheng@hit.edu.cn

Abstract

Recent advances in graph neural network (GNN)-based neural operators have demonstrated significant progress in solving partial differential equations (PDEs) by effectively representing computational meshes. However, most existing approaches overlook the intrinsic physical and topological meaning of higher-order elements in the mesh, which are closely tied to differential forms. In this paper, we propose a higher-order GNN framework that incorporates higher-order interactions based on discrete and finite element exterior calculus. The time-independent boundary value problems (BVPs) in electromagnetism are instantiated to illustrate the proposed framework. It can be easily generalized to other PDEs that admit differential form formulations. Moreover, the novel physics-informed loss terms, integrated form estimators, and theoretical support are derived correspondingly. Experiments show that our proposed method outperforms the existing neural operators by large margins on BVPs in electromagnetism. Our code is available at https://github.com/Supradax/Higher-Order-Differential-Topology-aware-GNN.

1 Introduction

Solving partial differential equations (PDEs) accurately is fundamental in scientific computations. Traditional numerical solvers [1] and the emerging physics-informed neural networks [2] rely on iterative computations. This is a significant bottleneck that precludes their application in time-sensitive domains where slight inaccuracy is tolerable but speed matters, such as gaming engines and interactive simulations. To address these limitations, neural operators [3–6] propose to directly learn the mapping between initial/boundary conditions and complete PDE solutions, eliminating time-consuming iterations while maintaining the capability to handle the PDEs whose exact analytical solutions are unattainable.

Convolutional neural network-based solvers are inherently constrained to regular, grid-like domains, whereas numerical solvers typically employ meshes to represent irregular solving regions—an approach naturally aligned with graph neural networks (GNNs). This compatibility has spurred growing interest in GNNs for time-dependent physics simulations, demonstrated through applications from fabric dynamics in wind [7] and granular particle systems [8] to neural mesh refinement schemes [9]. However, solving time-independent PDEs, especially boundary value problems (BVPs), presents greater challenges due to the absence of temporal guidance (initial data) and limited feature representation. Recent work [10] attempts to apply GNNs to BVPs in electromagnetism and has shown promising results, but is still limited to relatively simple cases.

Conventional GNN-based BVP solvers primarily utilize vertex adjacency in meshes while neglecting higher-order topological elements (edges, faces, cells), despite their fundamental physics interpretations from the perspective of differential forms [11]. While vector analysis has long dominated

*Corresponding Author.

39th Conference on Neural Information Processing Systems (NeurIPS 2025).

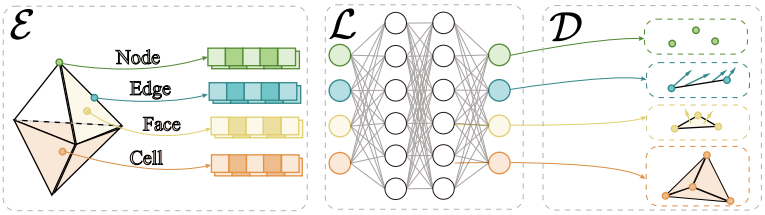

Figure 1: In the proposed DEC-HOGNN, scalar and vector fields on nodes, edges, faces and cells are encoded into k-simplex features, passing through HOGNN and decoded back as target fields.

physical modeling, modern physics recognizes that many vector fields are more naturally interpreted as differential forms on manifolds [12]. In electromagnetism, it reveals a hierarchical structure: potentials (φ) manifest as 0-forms, field intensities ($\mathbf{E}, \mathbf{H}$) as 1-forms, flux densities ($\mathbf{D}, \mathbf{B}$) as 2-forms and density distributions (ρ) as 3-forms [13]. This formalism, crystallized in the *Maxwell's House* representation of Maxwell's equations [14], treats traditional vector fields as mere proxies for underlying forms. Discrete exterior calculus [15] operationalizes this approach through De Rham mappings that represent k-forms as integrals over k-simplices [16]. Also, introducing geometric objects like differential forms allows us to naturally generalize this framework to PDEs on curved spaces [17] beyond merely incorporating topological structures [18, 19].

In this paper, we propose a higher-order GNN-based PDE solver framework by exploring the ideas in discrete exterior calculus (DEC) and finite element exterior calculus (FEEC) in a principled manner. By encoding the integrals over k-simplices as k-simplex features within higher-order GNNs (HOGNNs), which explicitly model interactions between simplices of varying dimensions, we establish a principled framework for solving form-based PDEs while preserving the topological and physical structure inherent to the problem domain. The resulting framework is dubbed DEC-HOGNN and illustrated in Figure 1. DEC-HOGNN enjoys better physical interpretation from the differential form perspective and can be extended to higher-dimension cases naturally. Our main contributions are summarized as follows: 1) We design a differential topology-aware HOGNN, which naturally encodes and decodes PDE operators based on the principles of DEC and FEEC. 2) Various physics-informed loss terms are derived under DEC-HOGNN, including the boundary condition ones, which can enable solving the boundary-value PDEs more effectively. 3) The universal approximation property in solving Poisson problems (electrostatics and magnetostatics) is presented, and the performance excellence is demonstrated via empirical experiments.

2 Related Work

Higher-Order GNNs. HOGNN is an extended learning framework on generalized graphs, i.e., hypergraphs [20]. A hypergraph G allows a hyperedge to contain more than two vertices [21]. HOGNN leverages the more abundant adjacencies on hypergraphs and mimics what GNN does on plain graphs via redefining various neighborhoods. If G has no further decorated structures, then one can define the k-node-tuple adjacency [22]; while boundary, co-boundary, upper, and lower adjacencies are available when G is a simplical complex [18] or a cell complex [23]. Mechanisms in GNN are mostly based on a special adjacency induced by edges and thus can be easily transplanted to hypergraphs. The graph-convolution [24], attention [25], and generalized message passing [26] of HOGNN all fall into this category. HOGNN has been well-studied in various regions, such as recommendation systems [27] and molecular predictions [28], where multi-body interactions are of significance, but beyond the expressive ability of plain graphs.

Neural Operators. Neural operator [3] learns function-to-function mappings mainly using data-driven loss instead of PDE-based physics loss. Its original implementation is furnished with kernel convolution of $O(n^2)$ complexity, which can be improved to $O(n \log n)$ in the spectral domain via discrete fast Fourier transform [3]. It is then extended to non-square-like regions [4] and spatial-spectral neural operators realized by wavelet transform [29–31]. This field later gradually shifts towards Transformer architectures with PDE-compatible attentions, from GNOT [5] employing boundary-aware cross-attention to Transolver [6] using attentions among domain slices.

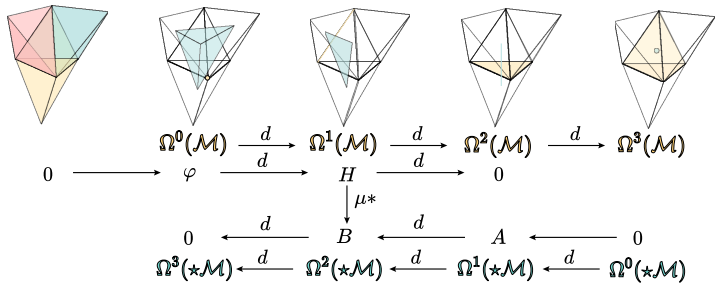

Figure 2: The primal manifold $\mathcal{M}$ has 4 tetrahedrals. The i-cell $\sigma_i \in \mathcal{M}$ $(i \in \{0, 1, 2, 3\})$ and its dual cell $\star\sigma_i$ are illustrated, associated with specific magnetic quantities. Identify the scalar potential φ as 0-form, vector potential $\mathbf{A}$ and magnetic intensity $\mathbf{H}$ as 1-form and magnetic flux density $\mathbf{B}$ as 2-form, and the relations $\mathbf{H} = \nabla\varphi, \mathbf{B} = \nabla \times \mathbf{A}, \nabla \times \mathbf{H} = \mathbf{0}, \nabla \cdot \mathbf{B} = 0$ are encoded into exterior derivative d and its property $d^2 = 0$. The electric case is similar.

GNN-based PDE Solvers. GNN-based neural operators have been studied in time-evolving mesh-based and particle-based physics simulations [7, 8]. The particles appear in the form of point clouds, and adjacency is built on local neighborhoods, in which equivariance is introduced to enhance model performance, such as subequivariance [32] and IsoGCN [33], an equivariant data-driven neural differential operator. To align with Neumann boundary in PDEs, NIsoGCN [34] further introduces a Neumann term into the differential kernel. This category requires data on fields and their differentials, but the latter is often intractable. It is found that message passing in GNNs can represent various numerical methods for time-dependent PDEs [35] and aligns with finite volume methods to achieve local mass conservation [36]. In addition, GNN-based approaches for BVPs [10] and inverse problems [37] are also explored.

3 Preliminary

De-Rham Mapping. In algebraic topology, a simplex chain complex $\mathcal{C}(X)$ on a topological space X is a graded vector space of k-order simplices $\mathcal{C}_k(X)$, decorated with the boundary operator ∂. A k-cochain $\sigma^k \in \mathcal{C}^k(X) : \mathcal{C}_k(X) \to \mathbb{R}$ is a real-valued function of $\sigma_k \in \mathcal{C}_k(X)$. If there exists a diffeomorphism φ between X and a smooth manifold $\mathcal{M}$, then for any k-form ω, we obtain a covariant functor mapping from $\mathcal{C}_k(X)$ to $\mathcal{C}^k(X)$, namely, De-Rham mapping [16]:

$$\mathcal{F} : \mathcal{C}_k(X) \to \mathcal{C}^k(X), \sigma_k \mapsto \int_{\varphi(\sigma_k)} \omega. \tag{1}$$

DEC and FEEC. *Discrete Exterior Calculus* (DEC) offers a comprehensive and differential topology-preserving toolkit to discretize operators on manifolds. In contrast to Graph Calculus [38], which treats a discretized manifold as a graph—at the cost of losing essential differential properties and thereby introducing inaccuracies—DEC maintains differential topology properties by working with integrations. Specifically, it characterizes a k-form $\omega \in \Omega^k(\mathcal{M})$ on a discrete manifold $\mathcal{M}$ through its integral over every k-simplex [16]. It yields high accuracy in applications where differential information matters, and is widely used in computational physics [39–42]. Another benefit of DEC is that it allows for processing manifolds from a dual perspective. For instance, the Hodge star $*^k : \Omega^k(\mathcal{M}) \to \Omega^{n-k}(\mathcal{M})$ on $\mathcal{M}$ gives the important constitution relation between $\mathbf{B}$ and $\mathbf{H}$ in electromagnetism. Even if $*^k\omega$ is intractable in the discrete case, we can still estimate its integral on the dual manifold $\star\mathcal{M}$ (shown in Figure 2) without a priori on the metric [15]. *Finite Element Exterior Calculus* (FEEC) generalizes the Finite Element Method (FEM) and is a numerical implementation of Galerkin methods. FEM is in essence an interpolation method with nodal functions, a.k.a., Lagrangian element [1]. However, such node-wise interpolation is inherently incompatible with differential operators such as div and curl, whereas the adoption of higher-order finite elements in FEEC enables the exact representation of these operators in the integral sense via straightforward linear combinations [14].

Whitney Element. Whitney elements are a type of finite elements used in FEEC and DEC. They provide a way to approximate differential forms on a discretized manifold that respects the geometry

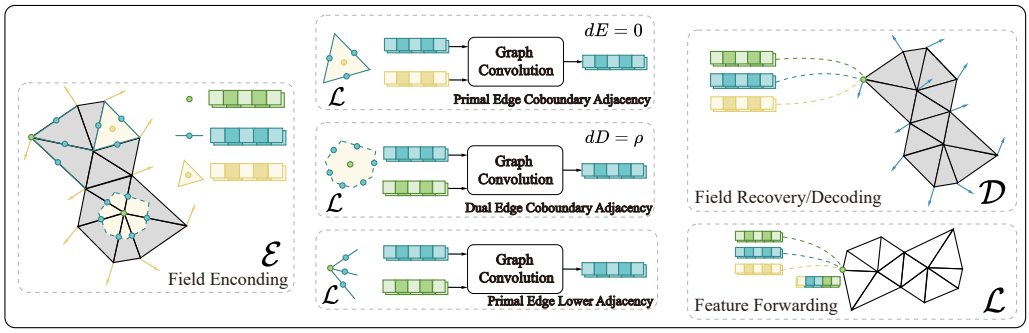

Figure 3: The illustration of DEC-HOGNN for 2D-electrostatics BVPs.

and topology of the manifold. Let w and $\mathbf{w}$ denote scalar and vector fields, respectively. Given a tetrahedralized mesh representation of a manifold $\mathcal{M}$ with $\dim \mathcal{M} = 3$, let $[i, j]$ denote the edge containing v_i, v_j and so are $[i, j, k], [i, j, k, l]$ for face and cell, respectively. The canonical node elements $\{w_i : w_i(v_j) = \delta_{ij}\}$ are functions on $\mathcal{M}$, in which δ_{ij} is the Kronecker delta. Let $W^0(\mathcal{M}), W^1(\mathcal{M}), W^2(\mathcal{M})$, and $W^3(\mathcal{M})$ denote the function spaces spanned by node elements w_i, edge elements $\mathbf{w}_{[i,j]}$, face elements $\mathbf{w}_{[i,j,k]}$, and cell elements $w_{[i,j,k,l]}$ (scalar fields), respectively. Then the integral of $\mathbf{w}_{[i,j]}$ along $[i, j]$, the flux of $\mathbf{w}_{[i,j,k]}$ through face $[i, j, k]$, and the volume integral of $w_{[i,j,k,l]}$ within tetrahedral $[i, j, k, l]$ all equal to 1 [14]. The element definitions are as follows:

$$\mathbf{w}_{[i,j]} := w_i \nabla w_j - w_j \nabla w_i \tag{2}$$

$$\mathbf{w}_{[i,j,k]} := 2(w_i(\nabla w_j \times \nabla w_k) + w_j(\nabla w_k \times \nabla w_i) + w_k(\nabla w_i \times \nabla w_j)) \tag{3}$$

$$w_{[i,j,k,l]} := 6 \sum_{\text{cyc}} w_i(\nabla w_j \times \nabla w_k) \cdot \nabla w_l = \chi_{\mathbf{x} \in [i,j,k,l]} / \operatorname{vol}([i, j, k, l]) \tag{4}$$

in which $w_i, w_j, w_k, w_l \in W^0(\mathcal{M})$. For ease of reference, the notation frequently used throughout the paper is summarized in Table 5 in Appendix A.

4 Methodology

Problem Setup and Motivation. In this work, we focus on PDEs that admit differential form formulation (many important PDEs in physics and engineering can be formulated using differential forms, such as Maxwell's, Navier-Stokes, Yang-Mills Equations, etc.). Given PDEs (often formulated in vector fields) on a discrete manifold $\mathcal{M}$, we aim to learn a neural operator $\mathcal{G}_\Theta$ that takes as inputs the observed scalar fields $\{s_i\}$ and vector fields $\{\mathbf{v}_i\}$, and outputs the target vector field $\mathbf{u}$ of interest:

$$\mathbf{u} = \mathcal{G}_\Theta(\{s_1, ..., s_m\}, \{\mathbf{v}_1, ..., \mathbf{v}_n\}, \mathcal{M}). \tag{5}$$

In comparison to the vector field formulation, the differential-form characterization of PDEs is coordinate-independent and explicitly reveals the geometric and topological aspects of the spaces. Motivated by this, we propose to transform the vector fields into the differential form formulation of the PDEs, which enables us to develop the neural operators by combining the principles in DEC and FEEC. The benefits are threefold: 1) they permit exploring the higher-order topological elements to facilitate PDE solving, 2) developing various physics-consistent losses, especially for the boundary-value problems, and 3) differential operators can be interpreted as simple linear combinations in DEC and FEEC, aligning with the higher-order message passing framework. Once the PDEs are solved, we then translate the results into the vector field language for downstream analysis.

Method Overview. Since differential k-forms can be represented as integrals on k-dimensional elements and further identified as higher-order element features, we introduce physics-informed higher-order interactions and aggregations into existing HOGNN frameworks in Section 4.1. Nevertheless, the initial input and expected output are often vectors instead of forms in practice. To circumvent this, we propose a proper encoder-decoder to enable consistent transformations in Section 4.2. In a nutshell, the input vectors are encoded into forms (higher-order features), processed by

HOGNN, and then decoded back into vectors, as illustrated in Figure 1. The physics-constrained loss and the universal approximation property of the proposed method are presented in Section 4.3.

As an illustrative example, we instantiate our framework by solving the classical BVPs in electromagnetism, and the proposed method can be easily generalized to other PDEs that can be formulated using differential forms. Recall that a typical Neumann electrostatic BVP is

$$\nabla \cdot \mathbf{D} = \rho, \nabla \times \mathbf{E} = \mathbf{0} \text{ in } \Omega;\ \mathbf{E} = \mathbf{E}_0, \mathbf{D} = \mathbf{D}_0 \text{ on } \partial\Omega;\ \mathbf{D} = \varepsilon_i \cdot \mathbf{E} \text{ in } \Omega_i, \tag{6}$$

in which $\rho, \mathbf{D}, \mathbf{E}$ are the charge density, displacement field, and electric field, respectively, whereas $\{\Omega_i\}$ is a partition of the domain Ω. The permittivity tensor ε_i can vary in different Ω_i consisting of different materials. In this case, the learned operator $\mathcal{G}_\Theta$ will take as input $(\{\rho\}, \{\mathbf{E}_0, \mathbf{D}_0\}, \Omega)$ and produce the complete fields $(\mathbf{E}, \mathbf{D})$. To this end, we rewrite Eq. 6 in its differential form formulation.

$$dD = \rho, dE = 0 \text{ in } \Omega;\ E = E_0, D = D_0 \text{ on } \partial\Omega;\ D = \varepsilon *^1 E \text{ in } \Omega_i, \tag{7}$$

in which $d\cdot$ denotes the exterior derivative and D, E are the corresponding k-forms. The input scalar field ρ and masked vector fields $\mathbf{E}, \mathbf{D}$ are first encoded into integrated forms in the form of vertex, edge and face features. Three types of edge adjacencies are used in the higher-order GNN, which give important physics interpretations (as shown in Figure 3): the curl-free property $dE = 0$ is implicitly included in the primal edge co-boundary adjacency, while Gauss's Law $dD = \rho$ is involved in the dual edge co-boundary adjacency. These GNN layers can be stacked sequentially, and the aggregated features can be either decoded back as complete $\mathbf{E}, \mathbf{D}$ or forwarded to other networks.

4.1 Physics-Informed Higher-Order Interactions

In light of DEC, we identify the potential on node, the circulation along an edge, the flux through a face, and the mass within a cell as the node, edge, face, and cell features, respectively. Given a discrete manifold $\mathcal{M}$ and its dual $\star\mathcal{M}$, since both of them are cell complexes, an element c onward have four types of neighborhood: boundary $\mathcal{B}(c) := \partial c$ and co-boundary $\mathcal{C}(c) := \{d : c \in \mathcal{B}(d)\}$, upper adjacency $\mathcal{N}_\uparrow(c) := \{d : \exists\delta, \{c, d\} \subset \mathcal{B}(\delta)\}$ and lower adjacency $\mathcal{N}_\downarrow(c) := \{d : \exists\delta, \{c, d\} \subset \mathcal{C}(\delta)\}$. Following the paradigm of [26], the element feature $\mathbf{h}'_c$ of c is updated by its original feature $\mathbf{h}_c$ and the aggregated messages from four neighborhoods $\mathcal{B}(c), \mathcal{C}(c), \mathcal{N}_\uparrow(c), \mathcal{N}_\downarrow(c)$ via:

$$\mathbf{h}'_c = \varphi\left(\mathbf{h}_c, \mathbf{m}_c^{\mathcal{B}}, \mathbf{m}_c^{\mathcal{C}}, \mathbf{m}_c^{\mathcal{N}_\downarrow}, \mathbf{m}_c^{\mathcal{N}_\uparrow}\right), \quad c \in \mathcal{M}, \tag{8}$$

$$\mathbf{m}_c^{\mathcal{B}} = \text{Aggregate}_{d\in\mathcal{B}(c)}\, \varphi_{\mathcal{B}}(\mathbf{h}_c, \mathbf{h}_d), \tag{9}$$

$$\mathbf{m}_c^{\mathcal{C}} = \text{Aggregate}_{d\in\mathcal{C}(c)}\, \varphi_{\mathcal{C}}(\mathbf{h}_c, \mathbf{h}_d), \tag{10}$$

$$\mathbf{m}_c^{\mathcal{N}_\uparrow} = \text{Aggregate}_{d\in\mathcal{N}_\uparrow(c),\ \delta\in\mathcal{C}(c)\cap\mathcal{C}(d)}\, \varphi_{\mathcal{N}_\uparrow}(\mathbf{h}_c, \mathbf{h}_d, \mathbf{h}_\delta), \tag{11}$$

$$\mathbf{m}_c^{\mathcal{N}_\downarrow} = \text{Aggregate}_{d\in\mathcal{N}_\downarrow(c),\ \delta\in\mathcal{B}(c)\cap\mathcal{B}(d)}\, \varphi_{\mathcal{N}_\downarrow}(\mathbf{h}_c, \mathbf{h}_d, \mathbf{h}_\delta). \tag{12}$$

Since forms in a PDE can be defined on both $\mathcal{M}$ and $\star\mathcal{M}$ (e.g., E and D in Eq. 7), we also propose a higher-order MPNN on the dual manifold $\star\mathcal{M}$ for dual forms by the fact:

$$\mathcal{B}(\star c) = \{\star d : d \in \mathcal{C}(c)\}, \quad \mathcal{C}(\star c) = \{\star d : d \in \mathcal{B}(c)\},$$
$$\mathcal{N}_\uparrow(\star c) = \{\star d : d \in \mathcal{N}_\downarrow(c)\}, \quad \mathcal{N}_\downarrow(\star c) = \{\star d : d \in \mathcal{N}_\uparrow(c)\}.$$

Usually, not all neighborhoods and elements will be used in higher-order MPNN due to computational complexity and the absence of features on corresponding elements. For instance, 2D-electrostatics BVPs only involve $\mathbf{E}, \mathbf{D}, \rho$ and thus only adjacencies about edges and faces are considered. In recent studies, there are various ways to implement the message passing on four different adjacencies, including generalized convolution, attention, and Transformer. We list several candidates of the adjacency layer backbones in Table 1 and will study their impact on model efficacy in Section 5.2.

In Table 1, $L^{(k)} := D - A = 2D - II^\top$ is the higher-order Laplacian [21], defined by indicator matrix $I_{ij} := \chi_{\sigma_i\in\mathcal{N}_\downarrow(\sigma_j)}$ and diagonal degree matrix D; $\tilde{L}$ is the Laplacian of an extended graph $G = (\mathcal{C}_k \cup \mathcal{C}_{k+1}, \{(c, d) : c \in \mathcal{C}_k, d \in \mathcal{C}(c)\})$; $\mathbf{h}_{c,d,\delta}$ is the concatenation of $\mathbf{h}_c, \mathbf{h}_d, \mathbf{h}_\delta$ and $\mathbf{h}_{c,d}$ is likewise. In our implementation, the relative orientation $\text{sign}(c, d)$ between two elements is further considered, via replacing $\mathbf{h}_{c,d}$ by $\text{sign}(c, d)\mathbf{h}_{c,d}$.

Consistency with Conservation Law. It is beneficial for solving BVPs by introducing higher-order interactions, because the interactions have meaningful physics interpretations, e.g., the sum of edge

Table 1: Possible implementations for co-boundary/lower adjacency layers.

Layer	Co-boundary and lower adjacencies
Convolution	$\mathbf{h}_c'^{(k)} = \sigma\big(\lvert\mathcal{N}_\downarrow(c)\rvert^{-\frac{1}{2}} \sum_{(d,\delta)\in\mathcal{N}_\downarrow(c)} \big(L^{(k)}\mathbf{h}^{(k)}\Theta^{(k)}\big)_d + \big(L^{(k+1)}\mathbf{h}^{(k+1)}\Theta^{(k+1)}\big)_\delta\big)$
	$\mathbf{h}_c'^{(k)} = \sigma\big(\lvert\mathcal{C}(c)\rvert^{-\frac{1}{2}} \sum_{d\in\mathcal{C}(c)} \big(\tilde{L}^{(k)}\mathbf{h}^{(k)}\Theta^{(k)}\big)_d\big)$
Attention	$\mathbf{h}_c' = \sigma(W_C\mathbf{h}_c + \sum_{(d,\delta)\in\mathcal{N}_\downarrow(c)} \mathrm{softmax}_{\mathcal{N}_\downarrow(c)}(\alpha_{d\delta})W_N\mathbf{h}_{c,d,\delta}), \alpha_{d\delta} = W_A\mathbf{h}_{c,d,\delta}$
	$\mathbf{h}_c' = \sigma(W_C\mathbf{h}_c + \sum_{d\in\mathcal{C}(c)} \mathrm{softmax}_{\mathcal{C}(c)}(\alpha_d)W_N\mathbf{h}_{c,d}), \alpha_d = W_A\mathbf{h}_{c,d}$
Transformer	$\mathbf{h}_c' = \sigma(W_C\mathbf{h}_c + \sum_{(d,\delta)\in\mathcal{N}_\downarrow(c)} \mathrm{softmax}_{\mathcal{N}_\downarrow(c)}(\lvert\mathcal{N}_\downarrow(c)\rvert^{-\frac{1}{2}}\mathbf{q}_c^\top\mathbf{k}_d)W_N\mathbf{h}_d)$
	$\mathbf{h}_c' = \sigma(W_C\mathbf{h}_c + \sum_{d\in\mathcal{C}(c)} \mathrm{softmax}_{\mathcal{C}(c)}(\lvert\mathcal{C}(c)\rvert^{-\frac{1}{2}}\mathbf{q}_c^\top\mathbf{k}_d)W_N\mathbf{h}_d)$

features around a face corresponds to the vorticity, while the sum of face features around a cell indicates the divergence at that location. This enables us to preserve structural conservation discretely by using integrated differential forms. Moreover, prior work also shows that adding conservation regularization can boost the performance of PDE solvers. For instance, a conservative GNN solver for 2D fluid dynamics [36] employs message passing based on face lower adjacency in the HOGNN framework and achieves local mass conservation (divergence-free) through asymmetric aggregation. We can realize more conservation constraints with DEC, e.g., enforcing vorticity conservation ($\nabla \times \mathbf{E} = 0$) and divergence conservation ($\nabla \cdot \mathbf{B} = 0, \nabla \cdot \mathbf{D} = \rho$) in electromagnetism.

Consistency with Electromagnetic Constitution Law. As a side-product, we can estimate the electric and magnetic permeability ε and μ of the medium while solving BVPs. The constitution law $\mathbf{B} = \mu\mathbf{H}, \mathbf{D} = \varepsilon\mathbf{E}$ can be equivalently interpreted by Hodge star: $B = \mu *^1 H, D = \varepsilon *^1 E$. It allows us to estimate the μ, ε along different directions via the definition in DEC:

$$\int_{\star\sigma_k} *^k\omega := \frac{\mathrm{vol}\,(\star\sigma_k)}{\mathrm{vol}\,(\sigma_k)} \int_{\sigma_k} \omega, \quad \omega \in \Omega^k(\mathcal{M}). \tag{13}$$

4.2 Encoder-Decoder between Vector Fields and Forms

Encoder. The encoder aims to transform vector fields into higher-order element features (integrated forms). In 3D-cases, a 1-form ω_1 and a 2-form ω_2 can be realized by *vector proxies* $\mathbf{u}_1$ and $\mathbf{u}_2$, with the aid of a unit tangent vector $\mathbf{t}$ on an edge σ_1 and a unit normal vector $\mathbf{n}$ on a face σ_2, respectively; while a 3-form ω_3 can be identified as a scalar field $u_3 : \mathbb{R}^3 \to \mathbb{R}$, and the integrated form is the usual volume integral. More formally,

$$\int_{\sigma_1} \omega_1 := \int_{\sigma_1} \mathbf{u}_1 \cdot \mathbf{t} ds, \quad \int_{\sigma_2} \omega_2 := \int_{\sigma_2} \mathbf{u}_2 \cdot \mathbf{n} dS, \quad \int_{\sigma_3} \omega_3 := \int_{\sigma_3} u_3 dV. \tag{14}$$

Given the samples $\{\mathbf{x}_j\}$ observed on σ_i ($i = 1, 2, 3$), the integrals on the right-hand sides of Eq. 14 can be estimated to yield the integrated forms numerically with either the Monte Carlo method or canonical quadrature rules on simplices (e.g., cubic quadrature on a triangle [43]). Similarly, the 2D case is given as follows and can be estimated similarly:

$$\int_{\sigma_1} w_1 = \int_{\sigma_1} \mathbf{u}_1 \cdot \mathbf{t} ds, \quad \int_{\sigma_2} w_2 := \int_{\sigma_2} u_2 dx dy. \tag{15}$$

In DEC, the differential forms in the primal manifold and dual manifold are related by the Hodge star $*^1$ (e.g., $E \in \Omega^1(\mathcal{M})$ and $D \in \Omega^2(\star\mathcal{M})$ in Eq. 7). Since we only have observations at primal nodes, it is simpler to estimate the integrated 2-forms on the primal manifold. However, DEC requires the integrals on the dual manifold, which poses a challenge for implementation. To sidestep this, we derive an approximation of the integrated dual forms based on the integrated primal forms, presented in Theorem 1. The details of the theorem can be found in Appendix C. Intuitively, the theorem offers us a simpler way to calculate the integrated dual forms.

Theorem 1 (Non-Cycle Forms Estimation)**.** *For a smooth k-form ω that is not a cycle defined on a bounded region, i.e., $d\omega$ does not vanish identically in any k-simplex σ_k, one can estimate the integrated dual forms $\{\int_{\star\sigma_{n-k}} \omega : \sigma_{n-k} \in \mathcal{C}_{n-k}(X)\}$ by using the integrated primal forms $\{\int_{\sigma_k} \omega : \sigma_k \in \mathcal{C}_k(X)\}$ up to accuracy $O(\varepsilon^{k+1})$ in which $\varepsilon := \sup_{\sigma_k \in \mathcal{C}_k(X)} \operatorname{diam} \sigma_k$.*

Decoder. The decoder intends to recover the vector fields from the derived integrated forms. The principle is that the integral of a proper vector field proxy on a simplex should equal the integrated form onward. To find the proxy at v_i for a 1-form (e.g., E in Eq. 7) along edge $[v_i, v_j]$, note that $h_{[v_i,v_j]}$—the final edge feature output by DEC-HOGNN—indicates the circulation of the proxy and the circulation of $\mathbf{w}_{[v_i,v_j]}$ in Eq. 2 along edge $[v_i, v_j]$ is 1, and thus the Whitney electric field contributed by edge $[v_i, v_j]$ at v_i is set to $h_{[v_i,v_j]}\mathbf{w}_{[v_i,v_j]}$. The contributions to v_i from different edges can be aggregated by average pooling or attention-style weighted sum. Similarly, for the proxies of 2-forms (e.g., D in Eq. 7) with final face feature $h_{[v_i,v_j,v_k]}$ and 3-forms (e.g., ρ in Eq. 7) with final cell feature $h_{[v_i,v_j,v_k,v_l]}$, the face and cell contribution are $h_{[v_i,v_j,v_k]}\mathbf{w}_{[v_i,v_j,v_k]}$ and $h_{[v_i,v_j,v_k,v_l]}w_{[v_i,v_j,v_k,v_l]}$ respectively, with $\mathbf{w}_{[v_i,v_j,v_k]}, w_{[v_i,v_j,v_k,v_l]}$ defined by Eq. 3 and Eq. 4.

Remark. The interpolation nature of the decoding approach offers a continuous field not only defined on the nodes but also in the cells. Though other GNN operators can also estimate the inner fields by multi-linear interpolation based on values at nodes, such methods can destroy certain important physical properties compared with Whitney elements. For instance, the reflection law in electrodynamics elucidates that the tangent component of $\mathbf{E}$ on the medium interface is continuous while the normal component is not. With prior knowledge of the interface positions, one can choose to average out contributions from each side respectively and obtain two different $\mathbf{E}$'s before and after reflection, which is consistent with physics on the interface, while a usual interpolation based on node-wise data cannot. Lastly, we present the theoretical analysis in Theorem 2, demonstrating that our encoding and decoding scheme preserves sufficient information for scalar and vector fields on a sufficiently fine mesh.

Theorem 2 (Proper Encoder-Decoder)**.** *Given a uniform partition $\{[x_i, x_{i+1}] : 1 \le i \le 2^N\}$ on the unit interval, i.e., $0 = x_1 < x_2 ... < x_{2^N+1} = 1$, the encoding operator $\mathcal{E}_N : W^{1,2}([0,1]) \to \mathbb{R}^{2^N}$ is defined as the 2^N integrals on each $[x_i, x_{i+1}]$ and the decoding operator $\mathcal{D}_N : \mathbb{R}^{2^N} \to C^\infty([0,1])$ maps any 2^N-dimensional feature $\mathbf{h}$ to a function $f(x)$ on $[0,1]$ such that $\int_{x_i}^{x_{i+1}} f(x)dx = \mathbf{h}_i$. Then for any $\varphi \in L^2([0,1])$ and $\varepsilon > 0$, there exists an integer $M > 0$ such that for all $N > M$,*

$$||\varphi - \mathcal{D}_N \circ \mathcal{E}_N(\varphi)||_{L^2} < \varepsilon. \tag{16}$$

By definition, we have $\mathcal{E}_N \circ \mathcal{D}_N = \mathrm{id}$.

4.3 Physics-Informed Loss and Universal Approximation Property

Physics-Informed Loss. Purely data-driven methods are likely to go against physics. Hence, PINN introduces physics-constrained loss as regularization to guide models to learn beyond the data resolution [44]. In PINN, the PDE residual is usually estimated by point-wise sampling and auto-differentiation. This is incompatible with GNNs since vertices are discrete, making it hard to enforce physics-consistency constraints, e.g., constraining a field to be curl-free [10]. But in integrated forms, one can interpret a differential version of PDEs into the integral version. For instance, magnetic flux density $\mathbf{B}$ is always divergence-free, inducing a DEC-version constraint:

$$dB = 0 \Leftrightarrow \nabla \cdot \mathbf{B} = 0 \Rightarrow \int_\Omega \nabla \cdot \mathbf{B} = \int_{\partial\Omega} \mathbf{B} \cdot \mathbf{n} = \sum_{\sigma_2 \in \partial\Omega} \int_{\sigma_2} \mathbf{B} \cdot \mathbf{n}_{\sigma_2} = \sum_{\sigma_2 \in \partial\Omega} \int_{\sigma_2} B = 0. \tag{17}$$

In our proposed framework, $\int_{\sigma_2} B$ is indeed a feature of face σ_2. Therefore, we can introduce physics-informed loss without sampling and differentiation, but by simply summing up corresponding higher-order features. More physics-informed loss terms are derived in Appendix B, covering the divergence, vorticity, and boundary conditions.

Universal Approximation Property. Theorem 3 shows the universal approximation ability of DEC-HOGNN in solving the Poisson problems. The proof is available in Appendix D.

Theorem 3 (Universal Approximation Property)**.** *Let $H^2(\Omega)$ denote the Hilbert space on a bounded closed region Ω with C^1-boundary, and $\mathcal{P}_i := \mathcal{D}_i \circ \mathcal{E}_i$ be the encoder-decoder projection with*

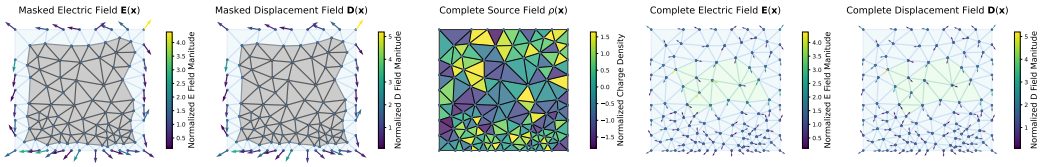

Figure 4: In the electrostatic field task, the model is required to output complete fields shown in the right-side two panels based on the left-side three panels.

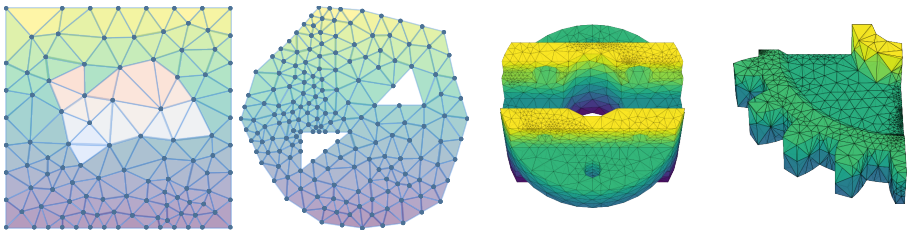

Figure 5: Models are compared on various settings. From left to right: 2D electrostatics BVP on a square 2D-mesh with two kinds of medium; 2D magnetostatics on an irregular holed mesh; 3D electrostatics and magnetostatics on a 3D socket model and a quarter-gear model, respectively.

resolution i. Given a simplex-partition $\{X_\alpha\}$ of Ω with measure-zero intersections, for any $f \in V \cup \bigcup_{i=1}^{\infty} \mathcal{P}_i V, V := H^2([0,1]^n) \cap \{f : ||\nabla f||_\infty < M\}$, there exists a network in the form of $\mathcal{D} \circ \mathcal{L}_N ... \circ \mathcal{L}_1 \circ \mathcal{E}$ with infinite neurons to solve the Dirichlet Poission problem on Ω, such that:

$$\lim_{\sup diam X_\alpha \to 0} ||\mathcal{D} \circ \mathcal{L}_N ... \circ \mathcal{L}_1 \circ \mathcal{E}(f, g) - u||_{L^2} = 0, \tag{18}$$

in which $\Delta u(\mathbf{x}) = f(\mathbf{x}), \mathbf{x} \in \Omega; u(\mathbf{x}) = g(x), \mathbf{x} \in \partial\Omega$.

As a corollary, note that $\mathbf{E} = \nabla u$ and the experiment setting below is equivalent to solving a Neumann boundary condition in a linear medium, the universal approximation property also rings true by a similar proof in Appendix D via single-layer potential method.

5 Experiment

5.1 Experiments and Benchmarks

Experiment Tasks. We assess the performance of the proposed model on 2D electric and magnetic boundary value problems. In the electrostatic case, the system is governed by a potential φ:

$$\Delta\varphi(\mathbf{x}) = \rho(\mathbf{x}), \mathbf{x} \in \Omega; \nabla\varphi(\mathbf{x}) = \mathbf{u}(\mathbf{x}), \mathbf{x} \in \partial\Omega,$$

which gives the electric intensity $\mathbf{E}$ and electric displacement $\mathbf{D}$. In our settings, the domain Ω is partitioned into two regions Ω_1, Ω_2 with measure-zero intersection. Ω_1 has isotropic permeability $\varepsilon_1 I$ while Ω_2 has a non-isotropic linear one ε_2, as shown in the blue and green-colored regions in Figure 4, and

$$\mathbf{D}(\mathbf{x}) = \varepsilon_i \mathbf{E}(\mathbf{x}), \mathbf{x} \in \Omega_i, i = 1, 2.$$

Let $H^2(\Omega)$ be the function space on Ω with L^2 derivatives, i.e., $H^2(\Omega) = \left\{f : ||f||_2^2 + ||\nabla f||_2^2 < \infty\right\}$ and $\mathbb{H}^2(\Omega)$ the vector-valued function space on Ω with $H^2(\Omega)$ components. The operator $\mathcal{G} : H^2(\Omega) \times \mathbb{H}^2(\partial\Omega)^2 \to \mathbb{H}^2(\Omega)^2, (\rho, \mathbf{E} \cdot \chi_{\mathbf{x}\in\partial\Omega}, \mathbf{D} \cdot \chi_{\mathbf{x}\in\partial\Omega}) \mapsto (\mathbf{E}, \mathbf{D})$ recovers the field $\mathbf{E}, \mathbf{D}$ on Ω based on prior knowledge on the boundary field data $(\mathbf{E}, \mathbf{D})$ on $\partial\Omega$ and the charge density distribution ρ on Ω, as shown in Figure 4.

Dataset Generation. Both 2D and 3D meshes are adopted as illustrated in Figure 5. The electrostatic data is obtained by FEM-based electromagnetism PDE solvers. Ω is partitioned into many triangles X_i with measure-zero intersections. The charge density ρ_i in each X_i is randomly assigned following a uniform distribution. The PDEs are then solved in a large enough vacuum region with Neumann boundary conditions. $\mathbf{E}, \mathbf{D}$ on boundary vertices and ρ on all vertices are sampled as input while

Table 2: Performance of different neural operators in terms of MSE. The bold and underscored numbers indicate the best and second-best in each column, respectively.

Model	2D Electrostatics	2D Magnetostatics	3D Electrostatics	3D Magnetostatics
DeepONet	1.866±0.025	1.438±0.021	0.842±0.094	0.483±0.001
MKGN	1.960±0.097	2.324±0.209	0.793±0.043	1.382±0.030
Galerkin-Type	1.209±0.028	1.895±0.144	1.176±0.030	**0.120±0.003**
GNOT	2.064±0.052	<u>1.142±0.149</u>	7.266±0.014	4.480±0.543
Transolver	2.751±0.009	7.432±0.143	8.249±0.009	7.089±0.460
GCN-based	1.362±0.015	1.224±0.026	1.986±0.892	0.182±0.009
GAT-based	1.360±0.014	1.755±0.040	1.029±0.049	1.222±0.021
Graph UNet-based	1.917±0.024	1.283±0.004	0.809±0.061	0.375±0.006
GT-based	<u>0.990±0.031</u>	1.405±0.077	<u>0.244±0.025</u>	0.171±0.023
DEC-HOGNN (**Ours**)	**0.623±0.058**	**0.875±0.052**	**0.195±0.005**	<u>0.158±0.008</u>

Table 3: Test loss and performance drop of different variants against the entire models.

Interactions	Lower adjacency	PD	P	D	None	PD	PD	PD	None
	Co-boundary	PD	PD	PD	PD	D	P	None	None
Test loss (mean square error)		0.652	0.676	0.678	0.719	0.954	0.959	1.244	2.077
Performance drop (%)		0.00	3.81	4.12	10.34	46.35	47.23	90.98	218.87

$\mathbf{E}, \mathbf{D}$ on all vertices are the target output. Scalar fields are normalized, and vector fields are shrunk with respect to the average norm to eliminate magnitude differences.

Note that the 2D magnetostatic field is also governed by a potential A_z (the vector potential $\mathbf{A}$ has only one non-vanishing component A_z if the 2D space is identified as the xy-plane). Therefore, the data generation is similar. For more details, please refer to Appendix E.

5.2 Numerical Results

Baselines and Implementation Details. To showcase the necessity of introducing specifically devised solvers for BVPs and the efficacy of the proposed method, we evaluate our model against the following general time-dependent PDE neural solvers, in which the input fields are masked accordingly: DeepONet [45], MKGN [46], Galerkin-type Attention [47], GNOT [5], and Transolver [6]; in addition, various GNN-based solvers devised particularly for BVPs are also included (as in [10]): GCN [48], GAT [49], Graph U-Net [50], and Graph-Transformer-based BVP solvers [51].

Main Results. Table 2 presents the MSE (mean square error) of different methods on 2D/3D electrostatics/magnetostatics BVPs. The neural operators from DeepONet to Transolver, which are mostly designed for time-dependent PDEs, yield larger errors compared with GNN-based BVP solvers. It is because many time-evolving PDE solvers like DeepONet predict an increment based on previous observations, which is unfortunately intractable in static cases. The multi-scale design in MKGN and the heterogeneous cross-attention in GNOT both suffer from the lack of features, as time-independent PDEs can be determined by the boundary conditions on boundary nodes, which takes up a minority. These make them no better than simple GNN operators in [10]. The proposed DEC-HOGNN considers implicit higher-order interactions in the governing systems and thereby outperforms usual GNN operators.

Ablation I: On Higher-Order Interactions. Different types of interactions can contribute variably to the performance of DEC-HOGNN. In this experiment, the full model incorporates four types of interactions, namely, primal and dual lower/co-boundary adjacencies, which are systematically ablated to evaluate their impact. The resulting variants are denoted as Primal-Dual (PD), Primal-only (P), Dual-only (D), and None. Table 3 presents the results in 2D electrostatic BVPs, which shows that message passing on edge lower adjacency brings minor enhancement while co-boundary adjacency matters much more. This result coincides with the governing PDE in electrostatics, $dE = 0, dD = \rho$, whose inducing loss terms are supposed to be computed based on both primal and dual co-boundary adjacency (Appendix B).

Table 4: The improvements of DEC-HOGNNs equipped with different higher-order graph convolutions and interactions against the vanilla GNN on the 2D-magnetostatics.

Backbone	GCN	GAT	Graph Transformer
Both co-boundary and lower adjacency	2.450±0.050	2.246±0.350	**1.222±0.036**
Lower adjacency only	3.463±0.069	3.491±0.081	1.629±0.068
Co-boundary only	2.159±0.045	**2.161±0.030**	1.386±0.041
Vanilla GNN	**1.876±0.038**	2.747±0.541	1.646±0.026
Improvement (%)	-15.07	21.33	25.75

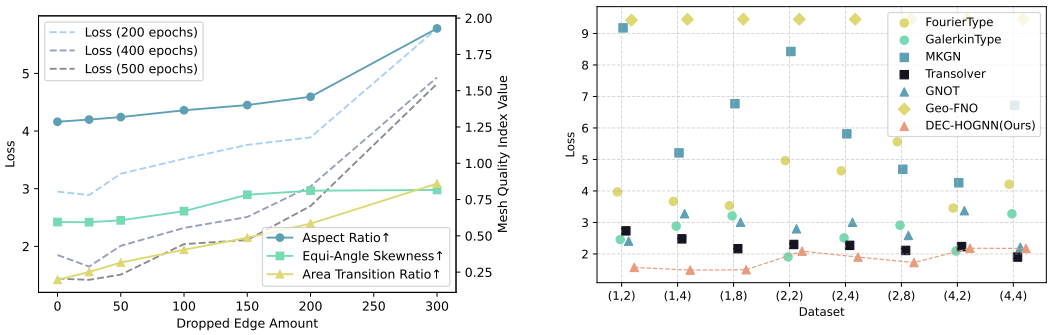

Figure 6: Left: Mesh quality and model performance of DEC-HOGNN variations as more edges are dropped; Right: Model comparison on meshes with different topological characteristics.

Ablation II: On Different GNN Backbones. In this experiment, we study the impact of different variants of higher-order GNNs on the efficacy of DEC-HOGNN by selecting different backbones, including GCN, GAT, and Graph Transformer (GT), on 2D electrostatic BVPs. Results in Table 4 manifest that higher-order interactions can enhance model performance (GAT and GT), which is consistent with the previous results. It further shows that adding more higher-order interactions does not necessarily imply more positive sides. For instance, the appearance of lower adjacency impedes GAT and GCN, while the co-boundary adjacency is much more beneficial for all backbones. Also, not every convolution can fit the DEC-HOGNN framework well just like the counterexample GCN.

Ablation III: On Performance Degeneration due to Mesh Quality. We analyze the negative impact out of mesh degradation by randomly dropping a certain amount of edges hierarchically. To measure the mesh quality quantitatively, three indicators are adopted with arrows implying degrading directions since good quality usually comes with uniform and regular elements. Further details on these tailored meshes are covered in Appendix E. The left panel of Figure 6 reflects that dropping edges from a triangularized mesh is followed by mesh degeneration. Also, minor degeneration would not affect the performance violently while a major one leads to salient performance drop. Note that it is also infeasible to adopt classical solvers using meshes with prominent quality issues. Thus these negative effects are tolerable.

Ablation IV: On Different Topological Characteristics. As shown in Figure 12, eight 2D magnetostatics benchmarks are used for the evaluation, which are named after their different topological properties by *(Connected Component Amount, Hole Amount)*. The right panel of Figure 6 shows that the advantage of our approach persists as the underlying topology changes.

6 Conclusion

In this paper, we propose a BVP solver via integrating higher-order topological interactions, which aligns with the discrete representation of differential forms, and the resulting model is aware of differential topology. Several novel physics-informed loss terms and integrated form estimators are also developed. Both theoretical analysis and experimental results demonstrate the advantages of incorporating higher-order interactions via integrated differential forms. Similar to traditional mesh-based numerical solvers, the performance of DEC-HOGNN is influenced by mesh quality, as Whitney elements may degrade on poorly shaped triangulated or tetrahedral meshes, potentially leading to convergence issues. Extending this approach to more general time-dependent PDEs and developing methods to mitigate mesh quality dependence are left for our future work.

Acknowledgements

This work is supported by the National Natural Science Foundation of China under Grant No. 62206074 and 62472125, Guangdong Basic and Applied Basic Research Foundation under Grant No. 2025A1515012932, Shenzhen College Stability Support Plan under Grant No. GXWD20220811173233001, Shenzhen Science and Technology Program No. JCYJ20241202123503005 and ZDSYS20230626091203008.

References

[1] Gouri Dhatt, Emmanuel Lefrançois, and Gilbert Touzot. *Finite element method*. John Wiley & Sons, 2012.

[2] Maziar Raissi. Deep hidden physics models: Deep learning of nonlinear partial differential equations. *Journal of Machine Learning Research (JMLR)*, 2018.

[3] Zongyi Li, Nikola Kovachki, Kamyar Azizzadenesheli, Burigede Liu, Kaushik Bhattacharya, Andrew Stuart, and Animashree Anandkumar. Fourier neural operator for parametric partial differential equations. In *International Conference on Learning Representations (ICLR)*, 2020.

[4] Zongyi Li, Daniel Zhengyu Huang, Burigede Liu, and Anima Anandkumar. Fourier neural operator with learned deformations for pdes on general geometries. *Journal of Machine Learning Research (JMLR)*, 2023.

[5] Zhongkai Hao, Zhengyi Wang, Hang Su, Chengyang Ying, Yinpeng Dong, Songming Liu, Ze Cheng, Jian Song, and Jun Zhu. GNOT: A general neural operator transformer for operator learning. In *Proceedings of the 40th International Conference on Machine Learning (ICML)*, 2023.

[6] Haixu Wu, Huakun Luo, Haowen Wang, Jianmin Wang, and Mingsheng Long. Transolver: A fast transformer solver for PDEs on general geometries. In *Proceedings of the 41st International Conference on Machine Learning (ICML)*, 2024.

[7] Tobias Pfaff, Meire Fortunato, Alvaro Sanchez-Gonzalez, and Peter Battaglia. Learning mesh-based simulation with graph networks. In *International Conference on Learning Representations (ICLR)*, 2021.

[8] Alvaro Sanchez-Gonzalez, Jonathan Godwin, Tobias Pfaff, Rex Ying, Jure Leskovec, and Peter Battaglia. Learning to simulate complex physics with graph networks. In *Proceedings of the 37th International Conference on Machine Learning (ICML)*, 2020.

[9] Ferran Alet, Adarsh Keshav Jeewajee, Maria Bauza Villalonga, Alberto Rodriguez, Tomas Lozano-Perez, and Leslie Kaelbling. Graph element networks: Adaptive, structured computation and memory. In *Proceedings of the 36th International Conference on Machine Learning (ICML)*, 2019.

[10] Winfried Lötzsch, Simon Ohler, and Johannes Otterbach. Learning the solution operator of boundary value problems using graph neural networks. In *ICML 2022 2nd AI for Science Workshop*, 2022.

[11] Barbara Burke Hubbard and John H. Hubbard. *Vector Calculus, Linear Algebra and Differential Forms: A Unified Approach*. Pearson, 2nd edition, 2001.

[12] Karl Warnick and Peter H. Russer. Differential forms and electromagnetic field theory. *Progress In Electromagnetics Research (PIER)*, 2014.

[13] Alain Bossavit. On the geometry of electromagnetism. *J. Japan Soc. Appl. Electromagn. & Mech*, 1998.

[14] Alain Bossavit. *Computational electromagnetism: variational formulations, complementarity, edge elements*. Academic Press, 1998.

[15] Anil Nirmal Hirani. *Discrete exterior calculus*. California Institute of Technology, 2003.

[16] Mathieu Desbrun, Eva Kanso, and Yiying Tong. Discrete differential forms for computational modeling. In *ACM SIGGRAPH 2006 Courses*. Birkhäuser Basel, 2006.

[17] Yunfeng Liao, Jiawen Guan, and Xiucheng Li. Curvature-aware graph attention for PDEs on manifolds. In *Forty-second International Conference on Machine Learning (ICML)*, 2025.

[18] Stefania Ebli, Michaël Defferrard, and Gard Spreemann. Simplicial neural networks. In *TDA & Beyond*, 2020.

[19] Mathieu Alain, So Takao, Brooks Paige, and Marc Peter Deisenroth. Gaussian processes on cellular complexes. In *Proceedings of the 41st International Conference on Machine Learning (ICML)*, volume 235, pages 879–905. PMLR, 2024.

[20] Maciej Besta, Florian Scheidl, Lukas Gianinazzi, Grzegorz Kwasniewski, Shachar Klaiman, Jürgen Müller, and Torsten Hoefler. Demystifying higher-order graph neural networks. *arXiv preprint arXiv:2406.12841*, 2024.

[21] Federico Battiston, Giulia Cencetti, Iacopo Iacopini, Vito Latora, Maxime Lucas, Alice Patania, Jean-Gabriel Young, and Giovanni Petri. Networks beyond pairwise interactions: Structure and dynamics. *Physics reports*, 2020.

[22] Christopher Morris, Martin Ritzert, Matthias Fey, William L. Hamilton, Jan Eric Lenssen, Gaurav Rattan, and Martin Grohe. Weisfeiler and leman go neural: Higher-order graph neural networks. *Proceedings of the AAAI Conference on Artificial Intelligence (AAAI)*, 2019.

[23] Cristian Bodnar, Fabrizio Frasca, Nina Otter, Yuguang Wang, Pietro Lio, Guido F Montufar, and Michael Bronstein. Weisfeiler and lehman go cellular: Cw networks. *Advances in neural information processing systems (NeurIPS)*, 2021.

[24] Eric Bunch, Qian You, Glenn Fung, and Vikas Singh. Simplicial 2-complex convolutional neural networks. In *TDA & Beyond*, 2020.

[25] Lorenzo Giusti, Claudio Battiloro, Lucia Testa, Paolo Di Lorenzo, Stefania Sardellitti, and Sergio Barbarossa. Cell attention networks. In *2023 International Joint Conference on Neural Networks (IJCNN)*, 2023.

[26] Cristian Bodnar, Fabrizio Frasca, Yuguang Wang, Nina Otter, Guido F Montufar, Pietro Lio, and Michael Bronstein. Weisfeiler and lehman go topological: Message passing simplicial networks. In *International conference on machine learning (ICML)*, 2021.

[27] Shiwen Wu, Fei Sun, Wentao Zhang, Xu Xie, and Bin Cui. Graph neural networks in recommender systems: a survey. *ACM Computing Surveys*, 2022.

[28] Wei Ju, Zequn Liu, Yifang Qin, Bin Feng, Chen Wang, Zhihui Guo, Xiao Luo, and Ming Zhang. Few-shot molecular property prediction via hierarchically structured learning on relation graphs. *Neural Networks*, 2023.

[29] Gaurav Gupta, Xiongye Xiao, and Paul Bogdan. Multiwavelet-based operator learning for differential equations. In *Advances in Neural Information Processing Systems (NeurIPS)*, 2021.

[30] Tapas Tripura and Souvik Chakraborty. Wavelet neural operator for solving parametric partial differential equations in computational mechanics problems. *Computer Methods in Applied Mechanics and Engineering*, 2023.

[31] Xiongye Xiao, Defu Cao, Ruochen Yang, Gaurav Gupta, Gengshuo Liu, Chenzhong Yin, Radu Balan, and Paul Bogdan. Coupled multiwavelet operator learning for coupled differential equations. In *International Conference on Learning Representations (ICLR)*, 2023.

[32] Jiaqi Han, Wenbing Huang, Hengbo Ma, Jiachen Li, Joshua B. Tenenbaum, and Chuang Gan. Learning physical dynamics with subequivariant graph neural networks. In *Advances in Neural Information Processing Systems (NeurIPS)*, 2022.

[33] Masanobu Horie, Naoki Morita, Toshiaki Hishinuma, Yu Ihara, and Naoto Mitsume. Isometric transformation invariant and equivariant graph convolutional networks. In *International Conference on Learning Representations (ICLR)*, 2021.

[34] Masanobu Horie and Naoto Mitsume. Physics-embedded neural networks: Graph neural pde solvers with mixed boundary conditions. *Advances in Neural Information Processing Systems (NeurIPS)*, 2022.

[35] Johannes Brandstetter, Daniel E. Worrall, and Max Welling. Message passing neural PDE solvers. In *International Conference on Learning Representations (ICLR)*, 2022.

[36] Masanobu Horie and Naoto Mitsume. Graph neural PDE solvers with conservation and similarity-equivariance. In *Forty-first International Conference on Machine Learning (ICML)*, 2024.

[37] Qingqing Zhao, David B. Lindell, and Gordon Wetzstein. Learning to solve PDE-constrained inverse problems with graph networks. In *ICML 2022 2nd AI for Science Workshop*, 2022.

[38] Matthias Hein, Jean-Yves Audibert, and Ulrike von Luxburg. Graph laplacians and their convergence on random neighborhood graphs. *Journal of Machine Learning Research (JMLR)*, 2007.

[39] Sharif Elcott, Yiying Tong, Eva Kanso, Peter Schröder, and Mathieu Desbrun. Stable, circulation-preserving, simplicial fluids. *ACM Transactions on Graphics (TOG)*, 2007.

[40] Pankaj Jagad, Abdullah Abukhwejah, Mamdouh Mohamed, and Ravi Samtaney. A primitive variable discrete exterior calculus discretization of incompressible navier–stokes equations over surface simplicial meshes. *Physics of Fluids (PoF)*, 2021.

[41] Pankaj Jagad and Ravi Samtaney. Effects of rotation on vorticity dynamics on a sphere with discrete exterior calculus. *Physics of Fluids (PoF)*, 2021.

[42] Patrick Mullen, Keenan Crane, Dmitry Pavlov, Yiying Tong, and Mathieu Desbrun. Energy-preserving integrators for fluid animation. *ACM Transactions on Graphics (TOG)*, 2009.

[43] G. R. Cowper. Gaussian quadrature formulas for triangles. *International Journal For Numerical Methods In Engineering*, 1973.

[44] Sifan Wang, Hanwen Wang, and Paris Perdikaris. Learning the solution operator of parametric partial differential equations with physics-informed deeponets. *CoRR*, 2021.

[45] Lu Lu, Pengzhan Jin, Guofei Pang, Zhongqiang Zhang, and George Em Karniadakis. Learning nonlinear operators via deeponet based on the universal approximation theorem of operators. *Nat. Mach. Intell.*, 2021.

[46] Zongyi Li, Nikola Kovachki, Kamyar Azizzadenesheli, Burigede Liu, Andrew Stuart, Kaushik Bhattacharya, and Anima Anandkumar. Multipole graph neural operator for parametric partial differential equations. In *Advances in Neural Information Processing Systems (NeurIPS)*, 2020.

[47] Shuhao Cao. Choose a transformer: Fourier or galerkin. In *Advances in Neural Information Processing Systems (NeurIPS)*, 2021.

[48] Xinzheng Xu, Xiaoyang Zhao, Meng Wei, and Zhongnian Li. A comprehensive review of graph convolutional networks: Approaches and applications. *Electronic Research Archive (ERA)*, 2023.

[49] Petar Veličković, Guillem Cucurull, Arantxa Casanova, Adriana Romero, Pietro Liò, and Yoshua Bengio. Graph attention networks. In *International Conference on Learning Representations (ICLR)*, 2018.

[50] Hongyang Gao and Shuiwang Ji. Graph u-nets. In *Proceedings of the 36th International Conference on Machine Learning (ICML)*, 2019.

[51] Seongjun Yun, Minbyul Jeong, Raehyun Kim, Jaewoo Kang, and Hyunwoo J. Kim. Graph transformer networks. In *Advances in Neural Information Processing Systems (NeurIPS)*, 2019.

[52] L.C. Evans. *Partial Differential Equations*. American Mathematical Society, 2nd edition, 2010.

[53] Loring W. Tu. *Differential Geometry: Connections, Curvature, and Characteristic Classes*. Springer, 1st edition, 2017.

[54] George Cybenko. Approximation by superpositions of a sigmoidal function. *Mathematics of Control, Signals and Systems (MCSS)*, 1989.

[55] Jonathan Richard Shewchuk. Delaunay refinement algorithms for triangular mesh generation. *Computational Geometry*, 22(1):21–74, 2002. ISSN 0925-7721. 16th ACM Symposium on Computational Geometry.

[56] Hang Si. Tetgen, a delaunay-based quality tetrahedral mesh generator. *ACM Transactions on Mathematical Software (TOMS)*, 2015.

NeurIPS Paper Checklist

1. **Claims**

   Question: Do the main claims made in the abstract and introduction accurately reflect the paper's contributions and scope?

   Answer: [Yes]

   Justification: The abstract and introduction are consistent with our actual contributions.

   Guidelines:

   - The answer NA means that the abstract and introduction do not include the claims made in the paper.
   - The abstract and/or introduction should clearly state the claims made, including the contributions made in the paper and important assumptions and limitations. A No or NA answer to this question will not be perceived well by the reviewers.
   - The claims made should match theoretical and experimental results, and reflect how much the results can be expected to generalize to other settings.
   - It is fine to include aspirational goals as motivation as long as it is clear that these goals are not attained by the paper.

2. **Limitations**

   Question: Does the paper discuss the limitations of the work performed by the authors?

   Answer: [Yes]

   Justification: In the Conclusion section, we discuss the limitation of the proposed framework, which can be affected by low mesh-quality.

   Guidelines:

   - The answer NA means that the paper has no limitation while the answer No means that the paper has limitations, but those are not discussed in the paper.
   - The authors are encouraged to create a separate "Limitations" section in their paper.
   - The paper should point out any strong assumptions and how robust the results are to violations of these assumptions (e.g., independence assumptions, noiseless settings, model well-specification, asymptotic approximations only holding locally). The authors should reflect on how these assumptions might be violated in practice and what the implications would be.
   - The authors should reflect on the scope of the claims made, e.g., if the approach was only tested on a few datasets or with a few runs. In general, empirical results often depend on implicit assumptions, which should be articulated.
   - The authors should reflect on the factors that influence the performance of the approach. For example, a facial recognition algorithm may perform poorly when image resolution is low or images are taken in low lighting. Or a speech-to-text system might not be used reliably to provide closed captions for online lectures because it fails to handle technical jargon.
   - The authors should discuss the computational efficiency of the proposed algorithms and how they scale with dataset size.
   - If applicable, the authors should discuss possible limitations of their approach to address problems of privacy and fairness.
   - While the authors might fear that complete honesty about limitations might be used by reviewers as grounds for rejection, a worse outcome might be that reviewers discover limitations that aren't acknowledged in the paper. The authors should use their best judgment and recognize that individual actions in favor of transparency play an important role in developing norms that preserve the integrity of the community. Reviewers will be specifically instructed to not penalize honesty concerning limitations.

3. **Theory assumptions and proofs**

   Question: For each theoretical result, does the paper provide the full set of assumptions and a complete (and correct) proof?

   Answer: [Yes]

Justification: The complete statement and proof can be found in Appendix D.

Guidelines:

- The answer NA means that the paper does not include theoretical results.
- All the theorems, formulas, and proofs in the paper should be numbered and cross-referenced.
- All assumptions should be clearly stated or referenced in the statement of any theorems.
- The proofs can either appear in the main paper or the supplemental material, but if they appear in the supplemental material, the authors are encouraged to provide a short proof sketch to provide intuition.
- Inversely, any informal proof provided in the core of the paper should be complemented by formal proofs provided in appendix or supplemental material.
- Theorems and Lemmas that the proof relies upon should be properly referenced.

4. **Experimental result reproducibility**

Question: Does the paper fully disclose all the information needed to reproduce the main experimental results of the paper to the extent that it affects the main claims and/or conclusions of the paper (regardless of whether the code and data are provided or not)?

Answer: [Yes]

Justification: Details on how to generate datasets for the conducted experiments are mentioned in Appendix E and experiment settings are also covered in Appendix F.

Guidelines:

- The answer NA means that the paper does not include experiments.
- If the paper includes experiments, a No answer to this question will not be perceived well by the reviewers: Making the paper reproducible is important, regardless of whether the code and data are provided or not.
- If the contribution is a dataset and/or model, the authors should describe the steps taken to make their results reproducible or verifiable.
- Depending on the contribution, reproducibility can be accomplished in various ways. For example, if the contribution is a novel architecture, describing the architecture fully might suffice, or if the contribution is a specific model and empirical evaluation, it may be necessary to either make it possible for others to replicate the model with the same dataset, or provide access to the model. In general. releasing code and data is often one good way to accomplish this, but reproducibility can also be provided via detailed instructions for how to replicate the results, access to a hosted model (e.g., in the case of a large language model), releasing of a model checkpoint, or other means that are appropriate to the research performed.
- While NeurIPS does not require releasing code, the conference does require all submissions to provide some reasonable avenue for reproducibility, which may depend on the nature of the contribution. For example
  (a) If the contribution is primarily a new algorithm, the paper should make it clear how to reproduce that algorithm.
  (b) If the contribution is primarily a new model architecture, the paper should describe the architecture clearly and fully.
  (c) If the contribution is a new model (e.g., a large language model), then there should either be a way to access this model for reproducing the results or a way to reproduce the model (e.g., with an open-source dataset or instructions for how to construct the dataset).
  (d) We recognize that reproducibility may be tricky in some cases, in which case authors are welcome to describe the particular way they provide for reproducibility. In the case of closed-source models, it may be that access to the model is limited in some way (e.g., to registered users), but it should be possible for other researchers to have some path to reproducing or verifying the results.

5. **Open access to data and code**

Question: Does the paper provide open access to the data and code, with sufficient instructions to faithfully reproduce the main experimental results, as described in supplemental material?

Answer: [Yes]

Justification: A repository containing data and code is provided in the abstract.

Guidelines:

- The answer NA means that paper does not include experiments requiring code.
- Please see the NeurIPS code and data submission guidelines (https://nips.cc/public/guides/CodeSubmissionPolicy) for more details.
- While we encourage the release of code and data, we understand that this might not be possible, so "No" is an acceptable answer. Papers cannot be rejected simply for not including code, unless this is central to the contribution (e.g., for a new open-source benchmark).
- The instructions should contain the exact command and environment needed to run to reproduce the results. See the NeurIPS code and data submission guidelines (https://nips.cc/public/guides/CodeSubmissionPolicy) for more details.
- The authors should provide instructions on data access and preparation, including how to access the raw data, preprocessed data, intermediate data, and generated data, etc.
- The authors should provide scripts to reproduce all experimental results for the new proposed method and baselines. If only a subset of experiments are reproducible, they should state which ones are omitted from the script and why.
- At submission time, to preserve anonymity, the authors should release anonymized versions (if applicable).
- Providing as much information as possible in supplemental material (appended to the paper) is recommended, but including URLs to data and code is permitted.

6. **Experimental setting/details**

   Question: Does the paper specify all the training and test details (e.g., data splits, hyperparameters, how they were chosen, type of optimizer, etc.) necessary to understand the results?

   Answer: [Yes]

   Justification: Details on how to generate datasets for the conducted experiments are mentioned in Appendix E and experiment settings are also covered in Appendix F.

   Guidelines:

   - The answer NA means that the paper does not include experiments.
   - The experimental setting should be presented in the core of the paper to a level of detail that is necessary to appreciate the results and make sense of them.
   - The full details can be provided either with the code, in appendix, or as supplemental material.

7. **Experiment statistical significance**

   Question: Does the paper report error bars suitably and correctly defined or other appropriate information about the statistical significance of the experiments?

   Answer: [Yes]

   Justification: The main results are reported with average and standard deviation error, as shown in Table 2 and Table 4. We conduct these experiments with at least three random seeds under each setting.

   Guidelines:

   - The answer NA means that the paper does not include experiments.
   - The authors should answer "Yes" if the results are accompanied by error bars, confidence intervals, or statistical significance tests, at least for the experiments that support the main claims of the paper.
   - The factors of variability that the error bars are capturing should be clearly stated (for example, train/test split, initialization, random drawing of some parameter, or overall run with given experimental conditions).
   - The method for calculating the error bars should be explained (closed form formula, call to a library function, bootstrap, etc.)

- The assumptions made should be given (e.g., Normally distributed errors).
- It should be clear whether the error bar is the standard deviation or the standard error of the mean.
- It is OK to report 1-sigma error bars, but one should state it. The authors should preferably report a 2-sigma error bar than state that they have a 96% CI, if the hypothesis of Normality of errors is not verified.
- For asymmetric distributions, the authors should be careful not to show in tables or figures symmetric error bars that would yield results that are out of range (e.g. negative error rates).
- If error bars are reported in tables or plots, The authors should explain in the text how they were calculated and reference the corresponding figures or tables in the text.

8. **Experiments compute resources**

   Question: For each experiment, does the paper provide sufficient information on the computer resources (type of compute workers, memory, time of execution) needed to reproduce the experiments?

   Answer: [Yes]

   Justification: See Appendix F.

   Guidelines:

   - The answer NA means that the paper does not include experiments.
   - The paper should indicate the type of compute workers CPU or GPU, internal cluster, or cloud provider, including relevant memory and storage.
   - The paper should provide the amount of compute required for each of the individual experimental runs as well as estimate the total compute.
   - The paper should disclose whether the full research project required more compute than the experiments reported in the paper (e.g., preliminary or failed experiments that didn't make it into the paper).

9. **Code of ethics**

   Question: Does the research conducted in the paper conform, in every respect, with the NeurIPS Code of Ethics `https://neurips.cc/public/EthicsGuidelines`?

   Answer: [Yes]

   Justification: We have read it and followed the NeurIPS Code of Ethics.

   Guidelines:

   - The answer NA means that the authors have not reviewed the NeurIPS Code of Ethics.
   - If the authors answer No, they should explain the special circumstances that require a deviation from the Code of Ethics.
   - The authors should make sure to preserve anonymity (e.g., if there is a special consideration due to laws or regulations in their jurisdiction).

10. **Broader impacts**

    Question: Does the paper discuss both potential positive societal impacts and negative societal impacts of the work performed?

    Answer: [No]

    Justification: Our work mainly focus on topics over scientific computation. It has no significant societial impacts.

    Guidelines:

    - The answer NA means that there is no societal impact of the work performed.
    - If the authors answer NA or No, they should explain why their work has no societal impact or why the paper does not address societal impact.
    - Examples of negative societal impacts include potential malicious or unintended uses (e.g., disinformation, generating fake profiles, surveillance), fairness considerations (e.g., deployment of technologies that could make decisions that unfairly impact specific groups), privacy considerations, and security considerations.

- The conference expects that many papers will be foundational research and not tied to particular applications, let alone deployments. However, if there is a direct path to any negative applications, the authors should point it out. For example, it is legitimate to point out that an improvement in the quality of generative models could be used to generate deepfakes for disinformation. On the other hand, it is not needed to point out that a generic algorithm for optimizing neural networks could enable people to train models that generate Deepfakes faster.
- The authors should consider possible harms that could arise when the technology is being used as intended and functioning correctly, harms that could arise when the technology is being used as intended but gives incorrect results, and harms following from (intentional or unintentional) misuse of the technology.
- If there are negative societal impacts, the authors could also discuss possible mitigation strategies (e.g., gated release of models, providing defenses in addition to attacks, mechanisms for monitoring misuse, mechanisms to monitor how a system learns from feedback over time, improving the efficiency and accessibility of ML).

11. **Safeguards**

    Question: Does the paper describe safeguards that have been put in place for responsible release of data or models that have a high risk for misuse (e.g., pretrained language models, image generators, or scraped datasets)?

    Answer: [NA]

    Justification: Models and data are used for scientific computation. There is no risk of misuse.

    Guidelines:

    - The answer NA means that the paper poses no such risks.
    - Released models that have a high risk for misuse or dual-use should be released with necessary safeguards to allow for controlled use of the model, for example by requiring that users adhere to usage guidelines or restrictions to access the model or implementing safety filters.
    - Datasets that have been scraped from the Internet could pose safety risks. The authors should describe how they avoided releasing unsafe images.
    - We recognize that providing effective safeguards is challenging, and many papers do not require this, but we encourage authors to take this into account and make a best faith effort.

12. **Licenses for existing assets**

    Question: Are the creators or original owners of assets (e.g., code, data, models), used in the paper, properly credited and are the license and terms of use explicitly mentioned and properly respected?

    Answer: [Yes]

    Justification: Appendix E depicts data details. Code and models are either original or open sources.

    Guidelines:

    - The answer NA means that the paper does not use existing assets.
    - The authors should cite the original paper that produced the code package or dataset.
    - The authors should state which version of the asset is used and, if possible, include a URL.
    - The name of the license (e.g., CC-BY 4.0) should be included for each asset.
    - For scraped data from a particular source (e.g., website), the copyright and terms of service of that source should be provided.
    - If assets are released, the license, copyright information, and terms of use in the package should be provided. For popular datasets, `paperswithcode.com/datasets` has curated licenses for some datasets. Their licensing guide can help determine the license of a dataset.
    - For existing datasets that are re-packaged, both the original license and the license of the derived asset (if it has changed) should be provided.

- If this information is not available online, the authors are encouraged to reach out to the asset's creators.

13. **New assets**

    Question: Are new assets introduced in the paper well documented and is the documentation provided alongside the assets?

    Answer: [Yes]

    Justification: The data on electromagnetic static fields will be uploaded to the repository. Their details can be found in Appendix E.

    Guidelines:

    - The answer NA means that the paper does not release new assets.
    - Researchers should communicate the details of the dataset/code/model as part of their submissions via structured templates. This includes details about training, license, limitations, etc.
    - The paper should discuss whether and how consent was obtained from people whose asset is used.
    - At submission time, remember to anonymize your assets (if applicable). You can either create an anonymized URL or include an anonymized zip file.

14. **Crowdsourcing and research with human subjects**

    Question: For crowdsourcing experiments and research with human subjects, does the paper include the full text of instructions given to participants and screenshots, if applicable, as well as details about compensation (if any)?

    Answer: [NA]

    Justification: Our work focuses on solving partial differential equations arising in math and physics and does not involve human subjects.

    Guidelines:

    - The answer NA means that the paper does not involve crowdsourcing nor research with human subjects.
    - Including this information in the supplemental material is fine, but if the main contribution of the paper involves human subjects, then as much detail as possible should be included in the main paper.
    - According to the NeurIPS Code of Ethics, workers involved in data collection, curation, or other labor should be paid at least the minimum wage in the country of the data collector.

15. **Institutional review board (IRB) approvals or equivalent for research with human subjects**

    Question: Does the paper describe potential risks incurred by study participants, whether such risks were disclosed to the subjects, and whether Institutional Review Board (IRB) approvals (or an equivalent approval/review based on the requirements of your country or institution) were obtained?

    Answer: [NA]

    Justification: Our work focuses on solving partial differential equations arising in math and physics and does not involve human subjects.

    Guidelines:

    - The answer NA means that the paper does not involve crowdsourcing nor research with human subjects.
    - Depending on the country in which research is conducted, IRB approval (or equivalent) may be required for any human subjects research. If you obtained IRB approval, you should clearly state this in the paper.
    - We recognize that the procedures for this may vary significantly between institutions and locations, and we expect authors to adhere to the NeurIPS Code of Ethics and the guidelines for their institution.

- For initial submissions, do not include any information that would break anonymity (if applicable), such as the institution conducting the review.

16. **Declaration of LLM usage**

    Question: Does the paper describe the usage of LLMs if it is an important, original, or non-standard component of the core methods in this research? Note that if the LLM is used only for writing, editing, or formatting purposes and does not impact the core methodology, scientific rigorousness, or originality of the research, declaration is not required.

    Answer: [No]

    Justification: The core of this paper does not involve LLM usage.

    Guidelines:

    - The answer NA means that the core method development in this research does not involve LLMs as any important, original, or non-standard components.
    - Please refer to our LLM policy (https://neurips.cc/Conferences/2025/LLM) for what should or should not be described.

Table 5: Summary of symbols and their corresponding meanings.

Symbol	Meaning
$\Omega^k(\mathcal{M})$	The space spanned by all k-form on manifold $\mathcal{M}$.
$\star\mathcal{M}$	The dual manifold of the primal manifold $\mathcal{M}$.
$\mathcal{C}(X)$	The simplex chain complex of topology space X.
$\mathcal{C}_k(X)$	The set of all k-simplices in $\mathcal{C}(X)$. Its element is denoted by σ_k.
$\mathcal{C}^k(X)$	The set of all k-cochain on $\mathcal{C}_k(X)$. $\forall\sigma^k \in \mathcal{C}_k(X), \sigma^k : \mathcal{C}_k(X) \to \mathbb{R}, \sigma_k \mapsto \sigma^k(\sigma_k)$.
$*^k$	The Hodge star acting on k-forms. $*^k : \Omega^k(\mathcal{M}) \to \Omega^{n-k}(\mathcal{M})$. In DEC, it maps k-forms on the discrete primal manifold to the discrete dual manifold, i.e., $*^k : \Omega^k(\mathcal{M}) \to \Omega^{n-k}(\star\mathcal{M})$
$[i_0, ..., i_n]$	A n-simplex with vertices $v_{i_0}, v_{i_1}, ..., v_{i_n}$ in order.
d^k	The exterior derivative. $d^k : \Omega^k(\mathcal{M}) \to \Omega^{k+1}(\star\mathcal{M})$.
∂^k	The boundary operator. $\partial^k : \mathcal{C}_k(X) \to \mathcal{C}_{k-1}(X)$.
$H^2(\Omega)$	The function space on region Ω with L^2 derivatives.
$\mathbb{H}^2(\Omega)$	The vector-valued function space on region Ω, each component having L^2 derivative.
$W^k(\mathcal{M})$	The space spanned by k-th order Whitney element defined on $\mathcal{M}$.
χ_A	Indicator function. $\chi_A = 1$ if condition A is satisified and otherwise $\chi_A = 0$.

A Notation

The notation used throughout the paper is summarized in Table 5.

B Training Loss Function Derivation

The loss below is under the assumption that the dual manifold is constructed based on circumcenters, and fields are recovered by interpolation. For brevity, we only focus on discrete manifolds in $\mathbb{R}^3$.

Div-free and Curl-free. $\nabla \cdot \mathbf{B} = 0 \Leftrightarrow dB = 0, B \in \Omega^2(\star\mathcal{M})$. By Stokes theorem,

$$0 = \int_{\sigma_3} dB = \int_{\partial\sigma_3} B = \sum_{\sigma_2 \prec \sigma_3} \int_{\sigma_2} B = \sum_{\sigma_2 \prec \sigma_3} \operatorname{sign}(\sigma_2)\mathbf{h}_{\sigma_2} \tag{19}$$

in which the partial-order relation $\sigma \prec \sigma'$ implies that σ is a face of σ'. And thus the physics-informed L^2 loss can be:

$$\mathcal{L}_{\text{div-free}} := \sum_{\sigma_3 \in \mathcal{M}} \left| \sum_{\sigma_2 \prec \sigma_3} \operatorname{sign}(\sigma_2, \sigma_3)\mathbf{h}_{\sigma_2} \right|^2 \tag{20}$$

Then for $\nabla \times \mathbf{H} = 0 \Leftrightarrow dH = 0, H \in \Omega^1(\mathcal{M})$, likewise, we have:

$$\mathcal{L}_{\text{curl-free}} := \sum_{\sigma_2 \in \star\mathcal{M}} \left| \sum_{\sigma_1 \prec \sigma_2} \operatorname{sign}(\sigma_1, \sigma_2)\mathbf{h}_{\sigma_1} \right|^2 \tag{21}$$

As for forms $\mathbf{D}, \mathbf{E}$ such that $\nabla \cdot \mathbf{D} = 0, \nabla \times \mathbf{E} = 0$, one can obtain the formula by modifying $\sigma_3 \in \mathcal{M}, \sigma_2 \in \star\mathcal{M}$ by $\sigma_3 \in \star\mathcal{M}, \sigma_2 \in \mathcal{M}$. And for brevity, we will only cover the case on $\star\mathcal{M}$ since that on $\mathcal{M}$ is almost the same. For non-divergence-free scenarios like $\nabla \cdot \mathbf{D} = \rho$, then the L^2 loss becomes:

$$\mathcal{L}_{\text{div}} := \sum_{\sigma_3 \in \star\mathcal{M}} \left| \rho(\sigma_3)\operatorname{vol}(\sigma_3) - \sum_{\sigma_2 \prec \sigma_3} \operatorname{sign}(\sigma_2, \sigma_3)\mathbf{h}_{\sigma_2} \right|^2 \tag{22}$$

Boundary Condition: $\mathbf{n} \cdot \mathbf{B} = 0$. Consider a tetrahedral $\sigma_3 := [A, B, C, D]$ with positive-oriented faces $[A, B, C], [C, D, A], [A, D, B], [B, D, C]$, as shown in Figure 7. Let h_A denote the altitude to the opposite face $[B, D, C]$ in σ_3, w_A the nodal function at vertex A, and similarly for the others.

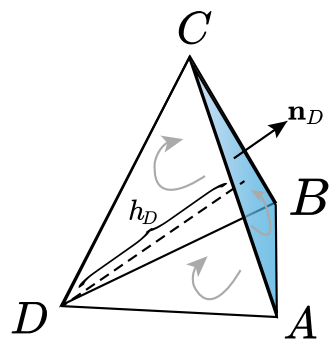

Figure 7: Tetrahedral $[A, B, C, D]$.

$\overrightarrow{AB}$ indicates the unit vector pointing from A to B. Let $H = h_A h_B h_C$, $H' = h_A h_B h_C h_D = H h_D$ and $V := \text{vol}(\sigma_3)$. Without loss of generality(WLOG), set $[A, B, C]$ to be the unique boundary face in σ_3 with outwards normal $\mathbf{n}_D$.

It can be easily shown that $-h_A \nabla w_A = \mathbf{n}_D$ [14] and the interpolation fields on $[A, B, C]$ only come from itself and its upper-adjacent neighbors. We first check whether its neighbors contribute normal components. WLOG, observe $[C, D, A]$ and we have:

$$\mathbf{w}_{[C,D,A]} \cdot \mathbf{n}_D = w_A(\nabla w_C \times \nabla w_D) \cdot \mathbf{n}_D + w_C(\nabla w_D \times \nabla w_A) \cdot \mathbf{n}_D + w_D(\nabla w_A \times \nabla w_C) \cdot \mathbf{n}_D = 0 \tag{23}$$

The first and second terms vanish since $-h_D \nabla w_D = \mathbf{n}_D$ while the last term vanishes since $w_D = 0$ on face $[A, B, C]$. Therefore, the only normal component contributor is $[A, B, C]$ itself and we have:

$$\int_{[A,B,C]} \mathbf{w}_{[A,B,C]} \cdot \mathbf{n}_D \, dS = 2 \int_{[A,B,C]} \sum_{\text{cyc}} w_A(\nabla w_B \times \nabla w_C) \cdot \mathbf{n}_D \, dS \tag{24}$$

$$= 2 \int_{[A,B,C]} \left(\frac{\cos\theta_A}{h_B h_C} w_A + \frac{\cos\theta_B}{h_C h_A} w_B + \frac{\cos\theta_C}{h_A h_B} w_C \right) dS \tag{25}$$

$$= \frac{2}{3} \text{vol}([A, B, C]) \left(\frac{\cos\theta_A}{h_B h_C} + \frac{\cos\theta_B}{h_C h_A} + \frac{\cos\theta_C}{h_A h_B} \right) \tag{26}$$

$$= \frac{2\text{vol}([A, B, C])}{3H} \sum_{\text{cyc}} h_A \cos\theta_A \tag{27}$$

in which θ_A is the intersection angle of $\overrightarrow{DA}$ and $\mathbf{n}_D$, cyc indicates the cyclic summation with respect to the tuple (A, B, C). Thus in the sense of average approximation, the loss on boundary condition $\mathbf{n} \cdot \mathbf{B} = 0$ is

$$\mathcal{L}_{\mathbf{n}\cdot\mathbf{B}} := \frac{4}{9} \sum_{\sigma_2 \in \partial_\star \mathcal{M}} \mathbf{h}_{\sigma_2}^2 \left| \frac{\text{vol}(\sigma_2)}{H_{\sigma_2}} \sum_{\text{cyc}} h_A \cos\theta_A \right|^2 \tag{28}$$

Boundary Condition: $\mathbf{n} \times \mathbf{H} = \mathbf{0}$. WLOG, assume only $[A, B]$ is on the boundary in σ_3 and it is obvious that the fields on $[A, B]$ comes from edges $\{\sigma_1' : \exists \sigma_2', \sigma_2, \sigma_1' \prec \sigma_2' \prec \sigma_3 \wedge \sigma_1 \prec \sigma_2 \prec \sigma_3\}$. First, observe that none in this set, except $[A, B]$ itself, has a tangential component contribution. WLOG,

$$\mathbf{w}_{[A,C]} \cdot \overrightarrow{AB} = (w_A \nabla w_C - w_C \nabla w_A) \cdot \overrightarrow{AB} = 0 \tag{29}$$

The first term vanishes since $\nabla w_C \cdot \overrightarrow{AB} = 0$ while the second vanishes since $w_C = 0$ on edge $[A, B]$. And thus the circulation on edge $[A, B]$ is:

$$\int_{[A,B]} \mathbf{w}_{[A,B]} \cdot \overrightarrow{AB} = \int_{[A,B]} (w_A \nabla w_B - w_B \nabla w_A) \cdot \overrightarrow{AB} \tag{30}$$

$$= \frac{\text{vol}([A, B])}{2} (\nabla w_B \cdot \overrightarrow{AB} + \nabla w_A \cdot \overrightarrow{BA}) \tag{31}$$

$$= \frac{\text{vol}([A, B])}{2} (\frac{\cos\theta_B}{h_B} + \frac{\cos\theta_C}{h_C}) \tag{32}$$

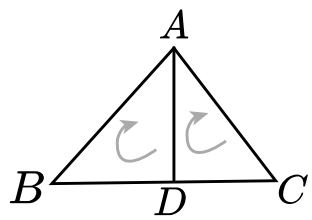

(a) Estimate the integrated dual 1-form on $[A, D]$ via integrated primal 1-forms on $\partial[A, B, C]$.

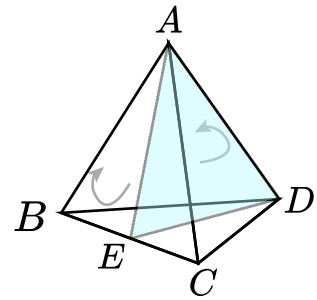

(b) Estimate the integrated dual 1-form on $[A, E, D]$ via integrated primal 1-forms on $\partial[A, B, C, D]$.

in which $\cos\theta_B = \mathbf{n}_B \cdot \overrightarrow{AB}$. Whence the corresponding loss is:

$$\mathcal{L}_{\mathbf{n}\times\mathbf{H}} := \frac{1}{4}\sum_{\sigma_1\in\partial\star\mathcal{M}} \mathbf{h}_{\sigma_1}^2 \left|\mathrm{vol}(\sigma_1)\sum_{v\in\partial\sigma_1}\frac{\cos\theta_v}{h_v}\right|^2. \tag{33}$$

Boundary Condition $\mathbf{n}\times\mathbf{B} = \mathbf{0}$. This condition is less common than $\mathbf{n}\cdot\mathbf{B} = 0$ in electromagnetism. It involves more terms since all faces of σ_3 have contributions. The term from $[A, B, C]$ is:

$$\vec{I}_{[A,B,C]} = 2\int_{[A,B,C]} w_A\frac{\cos\theta_A}{h_B h_C}\overrightarrow{HA} + w_A\frac{\cos\theta_B}{h_C h_A}\overrightarrow{HB} + w_A\frac{\cos\theta_C}{h_A h_B}\overrightarrow{HC} \tag{34}$$

$$= \frac{2\,\mathrm{vol}([A,B,C])}{3H}\sum_{\text{cyc}} h_A\cos\theta_A\overrightarrow{HA} \tag{35}$$

The terms from $[C, D, A]$, $[A, D, B]$, $[B, D, C]$ are respectively:

$$\vec{I}_{[A,B,C],[C,D,A]} = \frac{V}{h_D H}(h_A\overrightarrow{BA} + h_C\overrightarrow{BC}) \tag{36}$$

$$\vec{I}_{[A,B,C],[A,D,B]} = \frac{V}{h_D H}(h_B\overrightarrow{CB} + h_A\overrightarrow{CA}) \tag{37}$$

$$\vec{I}_{[A,B,C],[B,D,C]} = \frac{V}{h_D H}(h_C\overrightarrow{AC} + h_B\overrightarrow{AB}). \tag{38}$$

Thus, the loss is:

$$\mathcal{L}_{\mathbf{n}\times\mathbf{B}} := \sum_{\sigma_2\in\partial\star\mathcal{M}}\left|\mathrm{sign}(\sigma_2)\mathbf{h}_{\sigma_2}\vec{I}_{\sigma_2} + \sum_{\sigma_2\neq\sigma_2'\wedge\sigma_2,\sigma_2'\prec\sigma_3}\mathrm{sign}(\sigma_2')\mathbf{h}_{\sigma_2'}\vec{I}_{\sigma_2,\sigma_2'}\right|^2 \tag{39}$$

C Estimates among Integrated Forms

For a triangle region $[A, B, C]$ whose diameter is dominated by ε and a smooth function f, then direct expansion gives: $\forall\mathbf{x}\in[A, B, C]$,

$$\int_{[A,B,C]} f(\mathbf{x})dx = S_{[A,B,C]}f(\xi) = S_{[A,B,C]}f(\mathbf{x}) + S_{[A,B,C]}O(\varepsilon) = S_{[A,B,C]}f(\mathbf{x}) + O(\varepsilon^3) \tag{40}$$

And likewise,

$$\int_{[B,C]} f(\mathbf{x})dx = |BC|f(\mathbf{x}) + O(\varepsilon^2) \tag{41}$$

Let $|AB| := \mathrm{vol}([A, B])$ and assume that $|BD|/|DC| \gg \varepsilon$), then

$$\omega(\mathbf{x})\,\mathrm{vol}([A,B,D]) + O(\varepsilon^3) = \int_{[A,B,D]} d\omega = \int_{[A,B]}\omega + \int_{[B,D]} w + \int_{[D,A]}\omega \tag{42}$$

$$w(\mathbf{x}')\,\mathrm{vol}([A,C,D]) + O(\varepsilon^3) = \int_{[A,C,D]} dw = \int_{[A,C]} w + \int_{[C,D]} w + \int_{[D,A]} w \tag{43}$$

Note that $\omega(\mathbf{x}') = \omega(\mathbf{x}) + O(\varepsilon)$ and we have:

$$\frac{\int_{[A,B,D]} d\omega}{\int_{[A,C,D]} d\omega} = \frac{\mathrm{vol}([A,B,D]) + O(\varepsilon^3)}{\mathrm{vol}([A,C,D]) + O(\varepsilon^3)} = \frac{|BD| + O(\varepsilon^2)}{|DC| + O(\varepsilon^2)} = \frac{|BD|}{|DC|} + O(\varepsilon) \tag{44}$$

and

$$\frac{\int_{[A,B,D]} d\omega}{\int_{[A,C,D]} d\omega} = \frac{\int_{[A,B]} \omega + (|BD|/|BC|) \int_{[B,C]} \omega + \int_{[D,A]} \omega + O(\varepsilon^2)}{\int_{[A,C]} \omega - (|CD|/|BC|) \int_{[B,C]} \omega + \int_{[D,A]} \omega + O(\varepsilon^2)} \tag{45}$$

Combining Eq. 44 and Eq. 45 and rearranging the terms gives:

$$\int_{[A,D]} \omega = \frac{|BD|}{|BC|} \int_{[A,C]} \omega + \frac{|CD|}{|BC|} \int_{[A,B]} \omega + O(\varepsilon^2) \tag{46}$$

Likewise, one can mimic the process above and obtain the estimation of dual 2-forms by primal 2-forms:

$$\int_{[A,E,D]} \omega = \frac{|BE|}{|BC|} \int_{[A,C,D]} \omega + \frac{|CE|}{|BC|} \int_{[A,B,D]} \omega + O(\varepsilon^3). \tag{47}$$

This can be generalized to high-dimensional cases. For brevity, let $I(\sigma) := \int_\sigma \omega$ and $\tau_1 := [v_{i_0}, ..., v_{i_{n-2}}, u, w], \tau_2 := [v_{i_0}, ..., v_{i_{n-2}}, w, v]$ and we have:

$$O(\varepsilon) + \frac{\mathrm{vol}([u,w])}{\mathrm{vol}([w,v])} = \frac{\int_{\tau_1} d\omega}{\int_{\tau_2} d\omega} = \frac{\int_{\partial\tau_1} \omega}{\int_{\partial\tau_2} \omega} \tag{48}$$

, the right-hand side (RHS) equals:

$$\text{RHS} = \frac{\sum_{j=0}^{n-2} (-1)^j I_j(u,w) + (-1)^{n-1} I([v_{i_{1:n-2}}, w]) + (-1)^n I([v_{i_{1:n-2}}, u])}{\sum_{j=0}^{n-2} (-1)^j I_j(w,v) + (-1)^{n-1} I([v_{i_{1:n-2}}, v]) + (-1)^n I([v_{i_{1:n-2}}, w])} \tag{49}$$

$$= \frac{\sum_{j=0}^{n-2} (-1)^j \frac{\mathrm{vol}([u,w])}{\mathrm{vol}([w,v])} I_j(u,w) + (-1)^{n-1} I([v_{i_{1:n-2}}, w]) + (-1)^n I([v_{i_{1:n-2}}, u]) + O(\varepsilon^{n-1})}{\sum_{j=0}^{n-2} (-1)^j \frac{\mathrm{vol}([u,w])}{\mathrm{vol}([w,v])} I_j(w,v) + (-1)^{n-1} I([v_{i_{1:n-2}}, v]) + (-1)^n I([v_{i_{1:n-2}}, w]) + O(\varepsilon^{n-1})} \tag{50}$$

in which $I_j(u,w) = I([v_{i_{1:j-1,j+1:n-2}}, u, w]), I_j(w,v) = I([v_{i_{1:j-1,j+1:n-2}}, w, v])$. This gives:

$$\frac{\mathrm{vol}([u,w])}{\mathrm{vol}([w,v])} = \frac{(-1)^{n-1} I([v_{i_{1:n-2}}, w]) + (-1)^n I([v_{i_{1:n-2}}, u])}{(-1)^{n-1} I([v_{i_{1:n-2}}, v]) + (-1)^n I([v_{i_{1:n-2}}, w])} + O(\varepsilon^{n-1}) \tag{51}$$

$$= \frac{I([v_{i_{1:n-2}}, w]) - I([v_{i_{1:n-2}}, u])}{I([v_{i_{1:n-2}}, v]) - I([v_{i_{1:n-2}}, w])} + O(\varepsilon^{n-1}) \tag{52}$$

combine with the volume decomposition identity $\mathrm{vol}([u,w]) + \mathrm{vol}([w,v]) = \mathrm{vol}([u,v])$ and we have:

$$I([v_{i_{1:n-2}}, w]) = \frac{\mathrm{vol}([w,v])}{\mathrm{vol}([u,v])} I([v_{i_{1:n-2}}, u]) + \frac{\mathrm{vol}([u,w])}{\mathrm{vol}([u,v])} I([v_{i_{1:n-2}}, v]) + O(\varepsilon^{n-1}). \tag{53}$$

C.1 Estimate Integrated Dual Forms from Integrated Primal Forms

We only propose ways to estimate dual 1-forms in $\mathbb{R}^2$ and $\mathbb{R}^3$ and 2-forms from primal 1-forms and 2-forms since usual integration quadrature can be leveraged directly. Apart from that, we further show how to estimate dual 1-forms from primal 1-forms in $\mathbb{R}^n$. Higher-order estimates and higher dimensions are left for future work.

O is a non-overlappling vertex with vertices A, B, C s.t. $O \in \mathrm{span}[A, B, C]$. Specifically, if O is the dual node and the circumcenter of $[A, B, C]$, then $I([O, \star[B, C]]) = (I([O, B]) + I([O, C]))/2$. Therefore, it is reduced to show the relation between $I([O, X])$ and $I([X, Y])$ where $X, Y \in \{A, B, C\}$.

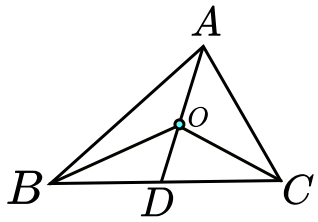

Figure 9: Estimate $\Omega^1(\star\mathcal{M})$ by $\Omega^1(\mathcal{M})$ in $\mathbb{R}^2$

Note that $I([A,O]) = \frac{\text{vol}([A,O])}{\text{vol}([A,D])} I([A,D])$ and $I([A,D])$ can be estimated by $I([A,B])$ and $I([A,C])$. And it appears done. However, it is possible to avoid introducing a new vertex D, in which case it is easier to extend to higher-dimensional cases. For brevity, let $S_A := \text{abs}(\text{vol}(B,C,O))$, $S := \text{vol}([A,B,C])$ and S_B, S_C is likewise defined.

$$\frac{\text{vol}([C,D])}{\text{vol}([B,C])} = \frac{\text{vol}([A,C,D])}{\text{vol}([A,C,B])} = \frac{\text{vol}([O,C,D])}{\text{vol}([O,C,B])} = \frac{S_B}{S_C + S_B} = \frac{S_B}{S - S_A} \tag{54}$$

And thus:

$$\begin{aligned} I([A,O]) &= \frac{\text{vol}([A,O])}{\text{vol}([A,D])} \left(\frac{\text{vol}([C,D])}{\text{vol}([B,C])} I([A,B]) + \frac{\text{vol}([B,D])}{\text{vol}([B,C])} I([A,C]) \right) \\ &= \frac{S - S_A}{S} \left(\frac{S_B}{S - S_A} I([A,B]) + \frac{S_C}{S - S_A} I([A,C]) \right) \\ &= \frac{S_B}{S} I([A,B]) + \frac{S_C}{S} I([A,C]) \end{aligned} \tag{55}$$

Combine with $I([O,\star[B,C]]) = (I([O,B]) + I([O,C]))/2$, we have:

$$I([O,\star[B,C]]) = \frac{S_A}{S} I([A,B]) + \frac{S_B - S_C}{S} I([B,C]) - \frac{S_A}{S} I([C,A]) \tag{56}$$

namely,

$$\begin{pmatrix} I[O,\star[B,C]]) \\ I[O,\star[C,A]]) \\ I[O,\star[A,B]]) \end{pmatrix} = \frac{1}{2S} \begin{pmatrix} S_A & S_B - S_C & -S_A \\ -S_B & S_B & S_C - S_A \\ S_A - S_B & -S_C & S_C \end{pmatrix} \begin{pmatrix} I([A,B]) \\ I([B,C]) \\ I([C,A]) \end{pmatrix} + O(\varepsilon^2) \tag{57}$$

However, this linear transform is not invertible since its determinant is zero. This implies that one cannot recover the integrated primal forms simply by this transform formula. We will later turn to this topic in Appendix C.2.

Fortunately, this formula can be easily extended to dimension n with the volume decomposition identity. For $\sigma_n = [v_0, ..., v_n]$ and $u \in \text{span}\,\sigma_n$, we have:

$$\sum_k (-1)^\tau \,\text{vol}([\tau(\sigma_{-k}), u]) = \text{vol}(\sigma_n) \tag{58}$$

in which $\sigma_{-k} := \sigma_n - \{v_k\}$ and τ is the permutation of the rest vertices. This can be easily verified by the identity Eq. 59, in which there are only n non-zero terms within 2^n terms in total.

$$\begin{aligned} \text{vol}(\sigma_n) &= \det(v_1 - v_0, v_2 - v_0, \ldots, v_n - v_0) \\ &= \det((v_1 - u) + (u - v_0), \ldots, (v_n - u) + (u - v_0)) \\ &= \sum_k (-1)^\tau \,\text{vol}([\tau(\sigma_{-k}), u]) \end{aligned} \tag{59}$$

Then we claim:

Theorem 4. *For a simplex $\sigma = (u, v, w_1, ..., w_n)$, $\forall o \in \text{int}\,\sigma$,*

$$I([u,o]) = \sum_{w \in \sigma_{-u}} \frac{\text{vol}([o, \sigma_{-w}])}{\text{vol}(\sigma)} I([u,w]) + O(\varepsilon^2). \tag{60}$$

Proof. WLOG, consider a simplex $\sigma = (u, v, w_1..., w_m)$, then for $o \notin \text{span}\{w_i\}$, then $\exists! p \in [w_{1:m}, v] \cap [u, o], q \in [w_{1:m}] \cap [v, p]$.

$$I([u,o]) = \frac{\text{vol}([u,o])}{\text{vol}([u,p])} I([u,p]) \tag{61}$$

$$= \frac{\text{vol}([u,o])}{\text{vol}([u,p])} \left(\frac{\text{vol}([p,q])}{\text{vol}([v,q])} I([u,v]) + \frac{\text{vol}([v,p])}{\text{vol}([v,q])} I([u,q]) \right) \tag{62}$$

$$= \frac{\text{vol}([u,o])}{\text{vol}([u,p])} \left(\frac{\text{vol}([p,q])}{\text{vol}([v,q])} I([u,v]) + \frac{\text{vol}([v,p])}{\text{vol}([v,q])} \sum_{w \in \sigma_{-v}} \frac{\text{vol}([\sigma_{-\{v,w\}}, q])}{\text{vol}([\sigma_{-\{v,w\}}, w])} I([u,w]) \right) \tag{63}$$

Whence we only need to check the coefficients in Eq. 60. We will use a property of vol. If $\text{span}\,\sigma = \text{span}\,\tau$ and $\text{vol}\,\sigma = \text{vol}\,\tau$, then for any simplex δ whose vertex is not in $\text{span}\,\sigma$, we have $\text{vol}([\sigma, \delta]) = \text{vol}([\tau, \delta])$.

The first term is:

$$\frac{\text{vol}([u,o])}{\text{vol}([u,p])} \frac{\text{vol}([p,q])}{\text{vol}([v,q])} = \frac{\text{vol}([u,o,q])}{\text{vol}([u,p,q])} \frac{\text{vol}([u,p,q])}{\text{vol}([u,v,q])} \tag{64}$$

$$= \frac{\text{vol}([u,o,q,\{w_i\}_{-k}])}{\text{vol}([u,v,q,\{w_i\}_{-k}])} \quad , \forall k \tag{65}$$

$$= \frac{\text{vol}([u,o,\{w_i\}])}{\text{vol}([u,v,\{w_i\}])} = \frac{\text{vol}([o,\sigma_{-v}])}{\text{vol}(\sigma)} \tag{66}$$

The second term is:

$$\frac{\text{vol}([u,o])}{\text{vol}([u,p])} \frac{\text{vol}([v,p])}{\text{vol}([v,q])} \frac{\text{vol}([\sigma_{-v-w}, q])}{\text{vol}([\sigma_{-v-w}, w])} = \frac{\text{vol}([u,o])}{\text{vol}([u,p])} \frac{\text{vol}([v,p,\sigma_{-w-v}])}{\text{vol}([v,q,\sigma_{-w-v}])} \frac{\text{vol}([\sigma_{-w}, q])}{\text{vol}([\sigma_{-v-w}, w])} \tag{67}$$

$$= \frac{\text{vol}([u,o])}{\text{vol}([u,p])} \frac{\text{vol}([p,\sigma_{-w}])}{\text{vol}\,\sigma} \tag{68}$$

$$= \frac{\text{vol}([o,\sigma_{-w}])}{\text{vol}\,\sigma} \tag{69}$$

This completes the proof.

By Eq. 60, we obtain all $I([u,o]), u \in \sigma$. But what about $I([\star\sigma_{-u}, o])$? Note that $[\star\sigma_{-u}, o] \subset [o, \sigma_{-u}]$ and thus we can apply Eq. 60 once again in $[o, \sigma_{-u}]$, denoted by τ_u. Consequently, we have:

$$I([o, \star\sigma_{-u}]) = -\sum_{v \in \tau_u} \frac{\text{vol}([(\tau_u)_{-v}, o])}{\text{vol}\,\tau_u} I([v,o]) + o(\varepsilon) \tag{70}$$

$$= -\sum_{v \in \tau_u} \sum_{w \in \sigma_{-v}} \frac{\text{vol}([(\tau_u)_{-v}, o])}{\text{vol}\,\tau_u} \frac{\text{vol}([\sigma_{-w}, o])}{\text{vol}\,\sigma} I([v,w]) + O(\varepsilon^2) \tag{71}$$

Note that for a simplex $\sigma = (x_1, ...x_m, u, v, w_1, ..., w_n)$, there exists and only exists one intersection p between (u, o) and $(v, w_{1:n})$ for all $o \in \text{int}\sigma$ and also only one q intersected at (v, p) and $(w_1, ..., w_m)$. Therefore, combine this result with Eq. 53, repeat the proof above and we have:

Corollary 5. *For a simplex $\sigma = (x_1, ...x_m, u, v, w_1, ..., w_n)$, $\forall o \in \text{int}\sigma$,*

$$I([x_{1:m}, u, o]) = \sum_{w \notin \{u, x_{1:m}\}} \frac{\text{vol}([o, \sigma_{-w}])}{\text{vol}(\sigma)} I([x_{1:m}, u, w]) + O(\varepsilon^{m+2}). \tag{72}$$

The estimation of dual 2-forms by primal 2-forms, as a special case, is:

$$I([A,E,D]) = \frac{\text{vol}([B,E])}{\text{vol}([B,C])} I([A,C,D]) + \frac{\text{vol}([C,E])}{\text{vol}([B,C])} I([A,B,D]) \tag{73}$$

$$I([A,E,D]) = \frac{\text{vol}([E,D])}{\text{vol}([D,H])} I([A,H,D]) = \frac{\text{vol}([E,D])}{\text{vol}([D,H])} \frac{\text{vol}([A,H])}{\text{vol}([A,O])} I([A,O,D]) \tag{74}$$

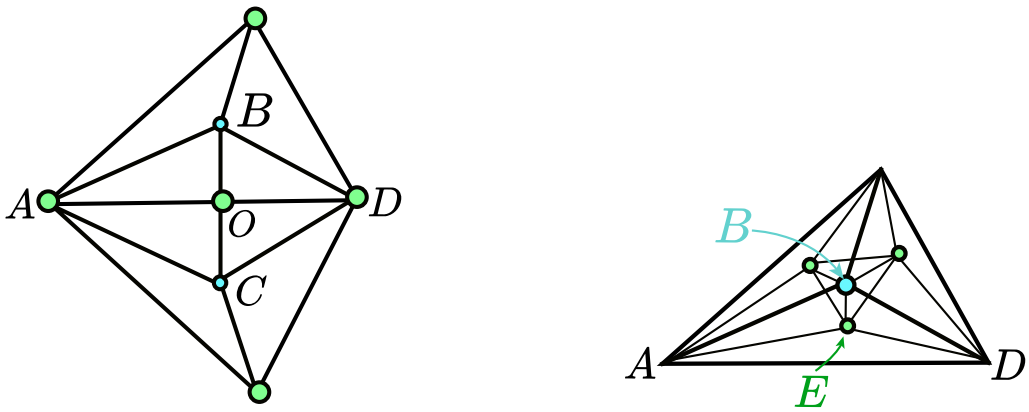

(a) Estimate primal forms by neighbors.

(b) Estimate primal forms by sub-division.

Figure 10: Illustrations for integrated primal form estimation.

$$I([A,O,D]) = \frac{\mathrm{vol}([A,O])}{\mathrm{vol}([A,H])}\frac{\mathrm{vol}([D,H])}{\mathrm{vol}([E,D])}\left(\frac{\mathrm{vol}([B,E])}{\mathrm{vol}([B,C])}I([A,C,D]) + \frac{\mathrm{vol}([C,E])}{\mathrm{vol}([B,C])}I([A,B,D])\right) \tag{75}$$

$$= \frac{\mathrm{vol}([A,O])}{\mathrm{vol}([O,H])}\frac{\mathrm{vol}([A,H])}{\mathrm{vol}([A,O])}\frac{V_B+V_C}{V}\left(\frac{V_C}{V_C+V_B}I([A,B,D]) + \frac{V_B}{V_C+V_B}I([A,C,D])\right) \tag{76}$$

$$= \frac{V_C}{V}I([A,B,D]) + \frac{V_B}{V}I([A,C,D]) \tag{77}$$

C.2 Estimate Integrated Primal Forms from Integrated Dual Forms

One may ask why we need to estimate the integrated primal forms by dual forms. After all, the dual manifold is not tetrahedralized and thus causes much more complexity in estimation. It stems from the intrinsic requirement in our previous proof. The approximation $\int_\sigma d\omega / \int_\tau d\omega \approx \mathrm{vol}\,\sigma / \mathrm{vol}\,\tau, x \in \sigma$ is fine if ω is **not exact**, i.e., $d\omega \neq 0$. Any exact forms cannot be properly estimated by the aforementioned quadratures.

But, fortunately, the converse estimation is a remedy to this limitation. Since $\int_{\star\sigma} d^*\omega / \int_{\star\tau} d^*\omega \approx \mathrm{vol}\,\star\sigma / \mathrm{vol}\,\star\tau$ fails if $d^*\omega = 0$. In smooth cases, forms on $\mathcal{M}$ are also forms on $\star\mathcal{M}$. If this also holds in the discrete cases, then by Hodge decomposition, the approximation is valid for any form up to a harmonic form.

Two methods can be applied: **sub-division** and **estimating from neighbors**. The latter has a default: it fails if this dual edge is on the boundary, i.e., it has no neighbors. For brevity, only estimating primal 1-forms from dual 1-forms in $\mathbb{R}^2$ is discussed, which, however, is not challenging to extend to higher-dimensional spaces and forms.

As shown in Figure 10a, given integrated dual forms, integrations of $[A,B], [B,D], [A,C], [C,D], [B,C]$ are all tractable. Then again by Stoke's theorem:

$$\frac{\mathrm{vol}([A,B,D])}{\mathrm{vol}([A,C,D])} \approx \frac{\int_{[A,B,D]} d\omega}{\int_{[A,C,D]} d\omega} = \frac{\int_{[A,B]}\omega + \int_{[B,D]}\omega + \int_{[D,A]}\omega}{\int_{[A,C]}\omega + \int_{[C,D]}\omega + \int_{[D,A]}\omega}, \tag{78}$$

in which $\int_{[A,D]}\omega$ can be estimated. But this approach fails when $[A,D]$ is on the boundary since such a quadrilateral $ABDC$ does not exist. Figure 10b offers another approach. By subdividing the primal triangles, note that $[A,D]$ is contained in both $[A,D,B]$ and $[A,D,E]$ where the integrated forms are known on every edge except $[A,D]$. Therefore, replace C in Eq. 78 by E and we obtain the estimate.

D Universal Approximation on Poission Equation

In this section, we show that for any properly exposed Dirichlet boundary value problems, there exists a proposed Higher-order GNN network that approximates the continuous operator. Our proof follows the famous result on the universal approximation property of neural networks for operator.

In our higher-order architecture, we encode the field vectors into differential forms and decode them via Whitney interpolation. Formally,

$$\mathrm{NN} = \mathcal{D} \circ \mathcal{L}_N ... \circ \mathcal{L}_1 \circ \mathcal{E} \tag{79}$$

in which $\mathcal{L}_i, \mathcal{E}, \mathcal{D}$ are the i-th layer, encoder layer and decoder layer, respectively. We first show that this encoding-decoding method has a pseudo-inverse property and an asymptotic identity property in a proper function space. First, we consider a simple but heuristic example, a real-valued function $\varphi \in W^{1,2}(I)$ on a closed interval $I \subset \mathbb{R}$. WLOG, $I := [0, 1]$.

Proof of Theorem 2.

Proof. The existence of $\mathcal{D}_N$ is trivial since for all $c \in \mathbb{R}$, there exists $a \in \mathbb{R}$ such that $\int_{x_i}^{(x_i+x_{i+1})/2} a((x_i + x_{i+1})/2 - x)dx + \int_{(x_i+x_{i+1})/2}^{x_{i+1}} a(x - (x_i + x_{i+1})/2) = c$. Since there are only finite non-smooth points, i.e., the interval endpoints and the midpoints, one can use a smooth mollifier there without changing the integral.

Recall the canonical mollifier $\eta_\varepsilon := \eta(x/\varepsilon)/\varepsilon$ [52] and $\varphi_\varepsilon := \eta_\varepsilon * f$. Since $\varphi \in H^2(I)$ is continuous, $\varphi_\varepsilon \to \varphi$ uniformly on the compact set I in the sense of L^2. Thus, we only need to show that $\varphi_\varepsilon \to \tilde{\varphi}$ in L^2. Since $\varphi_\varepsilon, \tilde{\varphi} \in C^\infty(I)$, we have $M_1 := \sup_{x\in I} \max\{\varphi'_\varepsilon(x), \tilde{\varphi}'(x)\} < \infty$ and $M_0 := \sup_{x\in I} \max\{\varphi(x), \tilde{\varphi}(x)\}$.

Direct expansion gives:

$$\int_{x_i}^{x_{i+1}} \varphi_\varepsilon(x)dx = \int_{x_i}^{x_{i+1}} \varphi_\varepsilon(s) + \varphi'_\varepsilon(\zeta_s)(x - s)dx = \varphi_\varepsilon(s)2^{-N} + \varphi'_\varepsilon(\zeta_s)\frac{(x_{i+1} - s)^2}{2} \tag{80}$$

Since $\varphi_\varepsilon \to \varphi$ uniformly, there exists ε small enough such that $\forall \varepsilon_0 > 0$,

$$\frac{\varepsilon_0}{2M_1} + \varphi_\varepsilon(s)2^{-N} + \varphi'_\varepsilon(\zeta_s)\frac{(x_{i+1} - s)^2}{2} = \tilde{\varphi}(t)2^{-N} + \tilde{\varphi}'(\zeta_t)\frac{(t - x_i)^2}{2}$$

which gives:

$$|\varphi_\varepsilon(s) - \tilde{\varphi}(t)| \le 2^N|\varphi'_\varepsilon(\zeta_s)|\frac{(x_{i+1} - s)^2}{2} + 2^N|\tilde{\varphi}'(\zeta_t)|\frac{(x_{i+1} - t)^2}{2} + \frac{\varepsilon_0}{2M_1} \tag{81}$$

$$\le 2 \cdot M_1 2^{-N-1} + \frac{\varepsilon_0}{2M_1} \tag{82}$$

$$< \delta + \frac{\varepsilon_0}{2M_1} \tag{83}$$

Thus $\exists N > \log_2 M_1/\delta$ such that $\forall s, t \in [x_i, x_{i+1}], |\varphi_\varepsilon(s) - \tilde{\varphi}(t)| < \delta$. Whence with $\delta = \varepsilon_0/2M_0$

$$\int |\varphi(x) - \tilde{\varphi}(x)|^2 dx \le \int |\varphi(x) - \varphi_\varepsilon(x)||\varphi(x) - \tilde{\varphi}(x)|dx + \int |\varphi_\varepsilon(x) - \tilde{\varphi}(x)||\varphi(x) - \tilde{\varphi}(x)|dx \tag{84}$$

$$\le 2M_0(\delta + \frac{\varepsilon_0}{2M_1}) + 2M_0\frac{\varepsilon_0}{2M_0} \tag{85}$$

$$= 3\varepsilon_0 \tag{86}$$

Corollary 6. *For uniformly bounded space $B_M([0, 1]) := \{\varphi \in L^2([0, 1]) : ||\varphi||_\infty < M\}$, $\forall \varphi \in B_M([0, 1])$, exists M such that for all $N > M$,*

$$||\varphi - \mathcal{D}_N \circ \mathcal{E}_N(\varphi)||_{L^2} < \varepsilon.$$

The proof can be analogously extended to higher dimension Ω with C^1 boundary by hypercube-partition.

Corollary 7. *Given a simplex-partition of* $[0,1]^d$ $\{X_\alpha\}$*with measure-zero intersections, for* $\mathbf{v} \in \mathbb{L}^2([0,1]^d) \cap \{\mathbf{u} : ||\mathbf{u}||_\infty < M\}$*,* $\mathcal{E}_N$ *encodes the line integral along every edge of* X_α *while* $\mathcal{D}_N$ *preserves them. Then there exists* δ *such that for* $\sup_\alpha diamX_\alpha < \delta$*,*

$$||\mathbf{u} - \mathcal{D}_\delta \circ \mathcal{E}_\delta(\mathbf{u})||_{L^2} < \varepsilon.$$

Proof. Consider a hypercube partition where the edges align with the coordinate axes. Therefore $\mathbf{u} \cdot \mathbf{t}_1$ can be viewed a function on x_1-axis, which is reduced to Theorem 1 and we have:

$$||\mathbf{u} - \mathcal{D}_N \circ \mathcal{E}_N(\mathbf{u})||_2 \leq \sum_{i=1}^{d} ||(\mathbf{u} - \mathcal{D}_N \circ \mathcal{E}_N(\mathbf{u})) \cdot \mathbf{t}_i||_2 < dM\varepsilon \tag{87}$$

Specifically, in $\mathbb{R}^3$, encoding $\mathbf{u}$ onto faces in the form of flux through the face is also proper since $\mathbf{u} \cdot \mathbf{n}_i$ is equivalent to encoding that to the edges. It is because faces are of codimension 1 in essence.

Define the projection operator $\mathcal{P}_N := \mathcal{D}_N \circ \mathcal{E}_N$. For $\mathcal{D}_N$, the degree of freedom of $\mathcal{D}_N$ is 2^N, and the interpolation is usually continuous with the encoded integral features in L^2-sense. And the integral operator $\mathcal{E}_N$ is continuous since $\mathcal{E}_N$ is linear and bounded, as the integral domain is compact. Therefore, $\mathcal{P}_N$ is continuous with proper interpolation.

Now consider the continuous functional family $C(K)$ on a compact set K. Let $V \subset\subset H^2(K) \cap B_M(K)$ in which $B(K) := \{f : K \to \mathbb{R} | |f'|_\infty < M\}$. By continuity, $\mathcal{P}_N V$ is still compact. Consider the space $W_N := V \cup \mathcal{P}_N V$ and $W := \bigcup_{i=0}^{\infty} W_i = V \cup \bigcup_{i=0}^{\infty} \mathcal{P}_i V$.

Lemma 8 (Arzela-Ascoli)**.** *X is a Banach space and $K \subset\subset X$. A subset V of $C(K)$ has compact closure if and only if V is uniformly bounded and equicontinuous.*

Theorem 9. *W is closed, uniformly bounded and equicontinous. By Arzela-Ascoli's lemma, W is compact.*

Proof. Consider a function sequence $\{f_n\}$. If $\{f_n\}$ has a subsequence in V, then it converges to f in V since V is compact. If $\{f_n\}$ has a subsequence $\{f_{i_n}\}$ such that $\sup_n i_n < M$, then it is again completed as the finite union preserves compactness. Therefore, we only need to consider the case $\{\mathcal{P}_{i_n} f_n\}$ in which $f_n \in V, i_n$ increasing to infinity. Note that $\{f_n\}$ must have a subsequence converging to g in V and thus:

$$||\mathcal{P}_{i_n} f_n - g||_2 \leq ||\mathcal{P}_{i_n} f_n - f_n||_2 + ||f_n - g||_2 < \delta/2 + \delta/2 < \delta \tag{88}$$

Thus $\lim_{n\to\infty} \mathcal{P}_{i_n} f_n = g$ a.e. W is bounded due to $|f'|_\infty < M$ and Poincaré inequality. W is equicontinuous if the interpolation is Lipschitz. For instance, the linear interpolation has a Lipschitz constant $2\sqrt{C}M$.

$$\left(\int_{x_i}^{x_{i+1}} f(x)dx\right)^2 \leq \int_{x_i}^{x_{i+1}} f(x)^2 dx \int_{x_i}^{x_{i+1}} 1^2 dx \tag{89}$$

$$\leq C2^{-N} \int_{x_i}^{x_{i+1}} f'(x)^2 dx \tag{90}$$

$$\leq CM^2 2^{-2N} \tag{91}$$

Whence functions in W are all Lipschitz and have a common upper bound $2\sqrt{C}M$ and are therefore equicontinuous. By Arzela-Ascoli Lemma, W is compact.

Consider a continuous convolution operator

$$\mathcal{G}[g](x) := \int_\Omega f(x-y)g(y)dy \tag{92}$$

and suppose that $\mathcal{G} : V \to W$, then we have:

$$||\mathcal{G}[g] - \text{NN}[g]||_2 = ||\mathcal{G}[g] - \mathcal{P}_n\mathcal{G}[g] + \mathcal{P}_n\mathcal{G}[g] - \mathcal{D} \circ \mathcal{L} \circ \mathcal{E}[g]||_2 \tag{93}$$

$$\leq ||\mathcal{G}[g] - \mathcal{P}_n\mathcal{G}[g]||_2 + ||\mathcal{P}_n\mathcal{G}[g] - \mathcal{D} \circ \mathcal{L} \circ \mathcal{E}[g]||_2 \tag{94}$$

$$\leq \sup_{h\in W} ||(I - \mathcal{P}_n)\mathcal{G}[h]||_2 + ||\mathcal{D} \circ (\mathcal{E} \circ \mathcal{G}[g] - \mathcal{L} \circ \mathcal{E}[g])||_2 \tag{95}$$

Note that W is compact and so is $\mathcal{G}W := \{\mathcal{G}[g] : g \in W\}$, therefore

$$\lim_{n\to\infty} \sup_{h\in W} ||(I - \mathcal{P}_n)\mathcal{G}[h]||_2 = 0$$

Note that in the linear interpolation scheme, $||\mathcal{D}(\mathbf{h}_1 - \mathbf{h}_2)||_2 = ||\mathbf{h}_1 - \mathbf{h}_2||_1$. Thus, the only thing to show is that $\mathcal{E} \circ \mathcal{G}[g] - \mathcal{L} \circ \mathcal{E}[g]$ can be bounded with a large enough N.

Theorem 10 (Green Function [52])**.** *The Green function of Poisson problem in $\mathbb{R}^n$ is:*

$$G(\mathbf{x}, \mathbf{y}) = \begin{cases} \frac{1}{(n-2)\alpha_n} \|\mathbf{x} - \mathbf{y}\|_2^{2-n}, & n \geq 3 \\ \frac{1}{2\pi} \ln \|\mathbf{x} - \mathbf{y}\|_2, & n = 2 \end{cases} \tag{96}$$

in which α_n is the surface area of a n-dimensional unit sphere and the solution for Dirichlet problem

$$\Delta u(\mathbf{x}) = f(\mathbf{x}), \mathbf{x} \in \Omega; u(\mathbf{x}) = g(\mathbf{x}) \equiv 0, \mathbf{x} \in \partial\Omega \tag{97}$$

is given by

$$u(\mathbf{x}) = \int_\Omega G(\mathbf{x} - \mathbf{y}) f(\mathbf{y}) dy - \int_{\partial\Omega} \partial_n G(\mathbf{x} - \mathbf{y}) g(\mathbf{y}) dy = \int_\Omega G(\mathbf{x} - \mathbf{y}) f(\mathbf{y}) dy \tag{98}$$

Lemma 11 (Extension Theorem [52])**.** *For a bounded closed Ω with C^1-boundary, there exists an extension operator $E : W^{1,p}(\Omega) \to W^{1,p}(\mathbb{R}^n)$, such that $E(u) = u$ in Ω and $E(u)$ is compactly supported and continuous:*

$$||Eu||_{W^{k,p}(\Omega)} \leq c_{n,\Omega} ||u||_{W^{k,p}(\Omega)} \tag{99}$$

For a bounded closed $\Omega \subset \mathbb{R}^n$, it must be paracompact and thus has a smooth partition of unity $\{\rho_\alpha\}$ [53]. For a square-like uniform mesh, one can construct a finite open cover $\{O_\alpha\}$ such that $\forall \delta > 0$, there exists a finite open cover $\sup_{\alpha\neq\beta} \operatorname{diam}(O_\alpha \cap O_\beta) < \delta$ and O_α contains the partitioned hypercube α. For those hypercubes not intersected with the boundary, the corresponding open covers can also have no intersections.

Recall that the extension theorem can be shown by the reflection method, in which we can locally extend a $u|_{O_i\cap\Omega} \equiv \rho_i u, \partial\Omega \subset \bigcup_{i=1}^K O_i$ due to the boundary compactness. It is obvious that

$$\mu(\text{supp}(Eu)) \geq \mu(\text{supp}(u)), \tag{100}$$

in which μ is the Lebesgue measure. And also note that

$$\begin{aligned}
\mu\big(\text{supp}(Eu)\big) &\leq \mu\Big(\text{supp}(u) \cup \text{supp}\Big(\sum_{i=1}^K \mathcal{R}_i[\rho_i u]\Big)\Big) && (101)\\
&\leq \mu\big(\text{supp}(u)\big) + \sum_{i=1}^K \mu\Big(\text{supp}\big(\mathcal{R}_i[\rho_i u]\big)\Big) && (102)\\
&= \mu\big(\text{supp}(u)\big) + \sum_{i=1}^K \mu\Big(\text{supp}(\rho_i u)\Big) && (103)\\
&\leq \mu\big(\text{supp}(u)\big) + \sum_{i=1}^K \mu\Big(\text{supp}(\rho_i)\Big) && (104)\\
&\leq \mu\big(\text{supp}(u)\big) + \delta_0 && (105)
\end{aligned}$$

in which $\mathcal{R}_i$ is the reflection operator concerning the open set O_i, and the last holds because ass the partition gets finer, the total volume of boundary hypercubes tends to be zero. Therefore, f defined on Ω can be extended to $\mathbb{R}^n$ such that $\int_\Omega G(\mathbf{y}) E[f](\mathbf{x} - \mathbf{y}) dy = \int_{\mathbb{R}^n} G(\mathbf{y}) E[f](\mathbf{x} - \mathbf{y}) dy + \varepsilon$. For brevity, we omit ε and identify $E[f]$ as f in the following discussion. Consider a component of

$\mathcal{E} \circ \mathcal{G}[g]$, i.e., the integral on I, and we have:

$$\int_I \int_\Omega G(\mathbf{x}-\mathbf{y}) f(\mathbf{y}) dy dx = \int_I \int_\Omega G(\mathbf{y}) f(\mathbf{x}-\mathbf{y}) dy dx \tag{106}$$

$$= \sum_J \int_I \int_J G(\mathbf{y}) f(\mathbf{x}-\mathbf{y}) dy dx \tag{107}$$

$$= \sum_J \int_I \int_J G(\mathbf{y}) f(\mathbf{x}-\mathbf{y}_J) - G(\mathbf{y}) \nabla f(\mathbf{x}-\zeta_J) \cdot (\mathbf{y}-\mathbf{y}_J) dy dx \tag{108}$$

$$= \sum_J \int_I f(\mathbf{x}-\mathbf{y}_J) dx \int_J G(\mathbf{y}) dy - \int_I \int_J G(\mathbf{y}) \nabla f(\mathbf{x}-\zeta_J) \cdot (\mathbf{y}-\mathbf{y}_J) dy dx \tag{109}$$

$$= \sum_J \int_{I+\mathbf{y}_J} f(\mathbf{x}) dx \int_J G(\mathbf{y}) dy - \int_I \int_J G(\mathbf{y}) \nabla f(\mathbf{x}-\zeta_J) \cdot (\mathbf{y}-\mathbf{y}_J) dy dx \tag{110}$$

$$=: \sum_J T_{1,I,J} + T_{2,I,J} \tag{111}$$

Note that $\int_I f(y)dy$ are components of $\mathcal{E}[g]$ and thus the neural network $\mathcal{L}$ is required to learn N^2 coefficients in the form of $\int_I f(x-y_J)dx$, a continuous function of x. But here the integral is on the translated I, i.e., $I + \mathbf{y}_J$ in the sense of Minkowski sum. Since f is extended to $\mathbb{R}^n$ such that $f = 0$ a.e. on $\mathbb{R}^n - \Omega$, we can omit those $I + \mathbf{y}_J$ not in the mesh. Therefore, encoding $f(y)$ as N^n integrals is still enough to estimate $T_{1,I,J}$.

For $T_{2,I,J}$, in sub-regions with $f(\mathbf{x})$ is not constant 0, as $N \to \infty$, we must have $|f(\mathbf{x})| > \delta$ due to continuity. Then we have

$$|T_{2,I,J}| \leq \int_J |G(\mathbf{y})| \cdot ||\nabla f(\mathbf{x}-\zeta_J)||_2 \cdot ||\mathbf{y}-\mathbf{y}_J|| dy \leq M \operatorname{diam}(J) \left| \int_J G(\mathbf{y}) dy \right| \tag{112}$$

Thus as $N \to \infty$, $\operatorname{diam}(J) \to 0 \Rightarrow T_{2,I,J} = o(\int_J G(\mathbf{y})dy)$ while $T_{1,I,J} = O(\int_J G(\mathbf{y})dy)$. We conclude that $T_{2,I,J} = o(T_{1,I,J})$ and therefore, we only need to focus on the main part. The first term can be interpreted as a matrix multiplication where $\mathcal{L}$ receives $x \in \Omega$ as the input and outputs $(N^n)^2$ coefficients. This can be approximated by the canonical universal approximation theorem [54]. This seemingly holds for special meshes, but in fact, one can adopt a bounded Jacobian to deform it into a more generalized mesh.

Note that the operator norm of $\mathcal{G}[f] := \int_\Omega G(\mathbf{x}-\mathbf{y}) f(\mathbf{y}) dy$ is finite as long as Ω is closed and bounded. Then by **Proper Encoder-Decoder** theorem, we reach Theorem 3. Following an analogous proof, one can see that it also holds for non-homogeneous Dirichlet conditions. Thus, we have the following corollary:

Corollary 12. *For non-homogeneous Dirichlet problems, $\Delta u(\mathbf{x}) = f(\mathbf{x}), \mathbf{x} \in \Omega; u(\mathbf{x}) = g(\mathbf{x}), \mathbf{x} \in \partial\Omega$, there also exists a network universally approximates u. Take gradients on both sides, there exists a network that universally approximates ∇u, i.e., the electric intensity* $\mathbf{E}$.

E Dataset Details

Table 6 lists out details of several benchmarks. 2D meshes are obtained by adding random points into a 2D convex hull and then triangulated via the open Python library *Triangle* [55]. 3D meshes come from example meshes provided by a free C++ tetrahedralization library *TetGen* [56].

2D cases. The 2D-electrostatics case involves triangle pieces constituting a square, including two media: silicon and a non-isotropic linear material. Each piece is assigned a random charge density excitation, and the region boundary condition is set as equal voltage. The 2D-magnetostatics case includes mu-metal (a material with a non-linear B-H curve) triangle pieces, composing an irregular mesh with two holes. Each triangle is randomly assigned a current density. The region boundary condition is *balloon*, implying an infinitely large region.

Table 6: Various meshes are adopted in different BVPs. ELE and MAG are for electrostatics and magnetostatics, respectively. NA means not applicable.

Mesh	Square	Holes	Socket	Gear
Vertex amount	105	180	2,407	2,453
Edge amount	277	487	12,865	12,833
Face amount	173	306	19,032	18,843
Cell amount	NA	NA	8,580	8,462
Train set size	120	120	240	240
BVP type	2D-ELE	2D-MAG	3D-ELE	3D-MAG

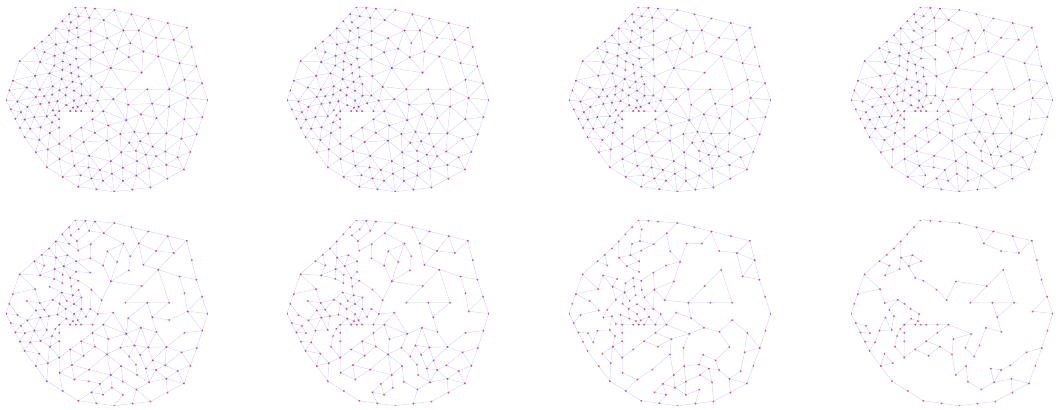

Figure 11: Illustrations of degraded meshes. The edge amount decreases from left to right and then from top to bottom.

Dropped Edge Amount	0	25	50	100	150	200	250	300
Vertex amount	180	180	180	180	177	168	155	114
Edge amount	487	462	437	387	334	275	216	139
Face amount	306	281	256	206	156	106	60	24
AR	1.286	1.301	1.318	1.365	1.401	1.458	1.595	1.929
EAS	0.595	0.594	0.607	0.670	0.783	0.811	0.975	0.816
ATR	0.197	0.251	0.316	0.404	0.487	0.584	0.657	0.860

Table 7: Details about the generated degraded meshes.

3D cases. The 3D-electrostatics case is an Al_2O_3-based socket, in which four SiO_2 cubic blocks are embedded with uniformly distributed random charge density. The solving region boundary condition is set to a uniform electric potential to simulate an enclosed empty cell in a metal. The 3D-magnetostatics case is a cobalt quarter-gear with three copper circuits with uniformly distributed random currents. The region boundary condition is that $\mathbf{H}$ is tangential to the boundary and the integral on the boundary vanishes.

All coordinates are normalized to $[0, 1]^d$, $d = 2, 3$, scalar fields are standardized, and vector fields are divided by average norm to eliminate scaling differences during pre-processing.

Degenerated Meshes via Dropping Edges. By randomly dropping a certain amount of edges and further deletion to fix the topology, these degraded meshes illustrated in Figure 11 and depicted in Table 6 are obtained. Usually, a mesh is considered having good quality if its elements are uniform and regular. We briefly introduce these three indicators here:

- **Aspect Ratio (AR)**. There are many versions of AR. We define it as the ratio between the maximum edge length over the minimum.

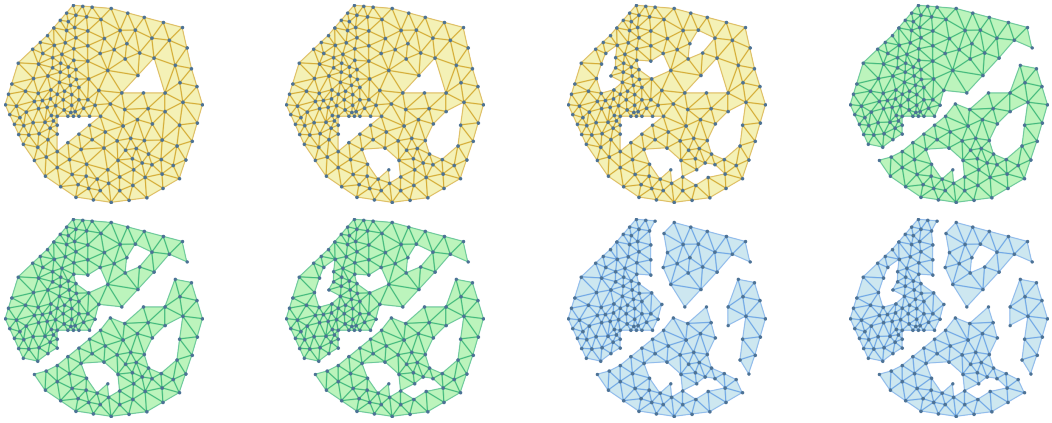

Figure 12: Illustrations of meshes with different topological characteristics. It is clear that those colored identically have the same connect compone

- **Equi-Angle Skewness (EAS)**. An N-polygon's ideal angle is $\theta = \pi(N-2)/N$. For an actual angle θ_i, its offset is $\delta_i := |\theta_i - \theta| / \max\{\theta, \pi - \theta\}$. And its EAS is $\max_i \delta_i$.
- **Area Transition Ratio (ATR)**. It depicts the uniformity of element size. Let A_i, A_j be the area of two neighboring elements. Then its ATR is $|A_i - A_j| / \max\{A_i, A_j\}$.

F Implementation Details

The hardware configuration consists of an Ubuntu 20.04 LTS operating system platform powered by four NVIDIA RTX A6000 Graphics Processing Units with 48GB memory. We use the PyTroch framework version 1.13 alongside Python 3.12 interpreter. Model optimization involved selection of the initial learning rate parameter γ for the Adam optimizer, which was systematically chosen from the discrete value set $\{i \times 10^{-j} : i \in \{1, 5\}, j \in \{1, 2, 3, 4, 5\}\}$ to achieve optimal performance metrics. Datasets are partitioned into training, validation, and test sets with the ratio 8:1:1. Each model in the main result is trained until the validation loss converges within 1,000 epochs.